Truncated radial glia as a common precursor in the late corticogenesis of gyrencephalic mammals

Running title: Binary fates of tRG in corticogenesis

Authors list

Merve Bilgic[1,2,3], Quan Wu[1,*],Taeko Suetsugu[1], Atsunori Shitamukai[1], Yuji Tsunekawa[1,4], Mitsutaka Kadota[5], Osamu Nishimura[5], Shigehiro Kuraku[5,6], Tomomi Shimogori[7], Hiroshi Kiyonari[8] and Fumio Matsuzaki[1,2,*]

Affiliations

[1]Laboratory for Cell Asymmetry, RIKEN Center for Biosystems Dynamics Research, Kobe, Hyogo 650-0047, Japan.

[2]Laboratory of Molecular Cell Biology and Development, Department of Animal Development and Physiology, Graduate School for Biostudies, Kyoto University, Kyoto 606-8501, Japan.

[5]Laboratory for Phyloinformatics, RIKEN Center for Biosystems Dynamics Research, Kobe, Hyogo 650-0047, Japan.

[7]Molecular Mechanisms of Brain Development, RIKEN Center for Brain Science, Wako, Saitama 351-0198, Japan.

[8]Laboratory for Animal Resources and Genetic Engineering, RIKEN Center for Biosystems Dynamics Research, Kobe, Hyogo 650-0047, Japan.

[*]Corresponding authors

quan.wu@riken.jp

fumio.matsuzaki@riken.jp

Further information and requests for resources and reagents should be directed to and will be fulfilled by the lead contact, Fumio Matsuzaki (fumio.matsuzaki@riken.jp)

Character count (excluding materials and methods, references, and figure legends): 32761

[3]Present address: The Institute for Quantitative Biosciences, The University of Tokyo, Tokyo 113-0033, Japan.
[4]Present address: Division of Molecular and Medical Genetics, Center for Gene and Cell Therapy, The Institute for Medical Science, The University of Tokyo, Tokyo 108-0071, Japan.
[6]Present address: Molecular Life History Laboratory, Department of Genomics and Evolutionary Biology, National Institute of Genetics, Mishima, Shizuoka 411-8540, Japan.

ABSTRACT

The diversity of neural stem cells is a hallmark of the cerebral cortex development in gyrencephalic mammals, such as Primates and Carnivora. Among them, ferrets are a good model for mechanistic studies. However, information on their neural progenitor cells (NPC), termed radial glia (RG), is limited. Here, we surveyed the temporal series of single-cell transcriptomes of progenitors regarding ferret corticogenesis and, despite the large timescale difference, found a conserved diversity and temporal trajectory between human and ferret NPC. We focused on truncated RG (tRG), a progenitor subtype previously described in humans. Results from time-lapse imaging in the ferret model suggest that tRG are generated from asymmetric apical divisions of RG sister cells. Moreover, the combination of *in silico* and *in vivo* analyses identified that tRG differentiate into both ependymal and astrogenic cells. Via transcriptomic comparison, we predict that this is also the case in humans. Our findings suggest that tRG play a role in the formation of adult ventricles, thereby providing the architectural bases for brain expansion.

Keywords:

Single-cell transcriptome / neural stem cell / brain development / ferret / human / neurogenesis / truncated radial glia.

INTRODUCTION

A vast diversity of neurons and glia form functional neural circuits during the development of the cerebral cortex in mammals. These cells are progressively generated from multipotent neural stem cells, termed radial glia (RG), following genetic processes common across species, from initially neurons of the deep layers (DL), then neurons of the upper layers (UL), and finally glial cells, astrocytes, or oligodendrocytes (**Fig. S1A, S1B**; Rowitch and Kriegstein, 2010). These processes are also spatially organized with RG divisions in the ventricular zone (VZ), IPC-neuron differentiation in the sub-VZ (SVZ), and neuron migration to the cortical plate in an inside-out manner. In many mammalian phylogenic states, cerebral carcinogenesis independently evolved to gain an additional germinal layer (outer SVZ (OSVZ); Smart et al, 2002), where extensive neurogenesis and gliogenesis of oRG occur (Fietz et al, 2010; Hansen et al, 2010) resulting in the amplification of neuronal and glial populations in the cortex (**Fig. S1**; Rash et al, 2019). On the other hand, a new subtype of NPC in the VZ has recently been reported in humans and rhesus macaques (deAzevedo et al, 2003; Nowakowski et al, 2016; Sidman and Rakic, 1973), lacking the basal attachment and is therefore termed truncated RG

(tRG). However, how widely tRG appears in gyrencephalic (or even lissencephalic) mammal development, what mechanisms underlie their formation, and what they produce remain unknown. As distinct NPC subtypes may possess different capacities to generate differentiated progenies (Huang et al, 2020; Rash et al, 2019), it would be critical to find answers to those questions to understand commonality and diversity in the mammalian brain evolution.

Genetic manipulation of individual cell types *in vivo* and single-cell transcriptome analysis are two major and successful approaches in revealing the properties of cells, such as their proliferation and differentiation. Thus, single-cell RNA sequencing (scRNA-seq) of the human brain during development has been extensively performed (Bhaduri et al, 2020, 2021; Huang et al, 2020; Johnson et al, 2015; Liu et al, 2017; Polioudakis et al, 2019; Pollen et al, 2015; Zhong et al, 2018). However, the *in vivo* behavior in humans and other primates and the underlying mechanisms remain less explored owing to the limited experimental access to the developing primate cortices. Particularly, resources available for the late human embryonic brain are extremely rare due to ethical challenges. Also, studies using brain organoids face issues in recapitulating the specification and maturation of cell types during human brain development (Bhaduri et al, 2020). In this context, the ferret (*Mustela putorius furo*) is highlighted as a suitable animal model, which compensates for the difficulties in studying human cortical development. Ferrets are carnivores that develop common gyrencephalic features, such as the OSVZ and a folded brain, and are frequently used in mammalian models of brain development and circuit formation because neurogenesis continues in their early neonatal stages. Since this species is experimentally manipulable, recent studies have developed *in vivo* gene manipulation and editing technology using *in utero* electroporation (IUE; Matsui et al, 2013; Kawasaki et al, 2012; Tsunekawa et al, 2016). Furthermore, ferrets showed severe microcephalic phenotypes via *ASPM* (*Abnormal Spindle-like Microcephaly-associated* gene) knockout (Johnson et al, 2018; Kou et al, 2015), which greatly differs from a minor phenotype in mouse *ASPM* knockout mutants (Capecchi and Pozner, 2015; Fujimori et al, 2014; Jayaraman et al, 2016; Pulvers et al, 2010). This remarkable finding suggests the presence of mechanisms underlying brain enlargement and circuit complexity shared by gyrencephalic species to some extent. Results from transcriptome profiling of ferret cortical cells has revealed regional differences in germinal layers and cell-type composition (Johnson et al, 2018; de Juan Romero et al, 2015). However, because of the incomplete genomic information, especially due to the lack of genetic models, the databases with ferret data have been less reliable than those with human or mice data. This has posed a limit for the accurate

comparison of single cell transcriptomes between ferrets and humans. Hence, the temporal pattern of molecular signatures of ferret NPC remains largely unexplored at single-cell resolution. Comparison of progenitor subtypes and sequential events at the single-cell transcriptome level regarding development between ferrets and humans will greatly help to recognize common and species-specific mechanisms underlying the construction of a complex brain.

In this study, we comprehensively analyzed the developmental dynamics of progenitor populations during ferret corticogenesis to clarify shared or species-specific mechanisms of corticogenesis in gyrencephalic mammals and found that ferrets generate tRG at late neurogenic and early gliogenic stages like humans and other primates. Analysis of the pseudotime trajectory and temporal histochemical pattern suggested that tRG generate ependymal and astrogenic cell fates. Then, we compared temporal series of ferret and human single cell transcriptomes (Bhaduri et al, 2021; Nowakowski et al, 2017). Remarkably, we found homologous temporal progenitor trajectories irrespective of the large differential corticogenesis timescale. This study combining rich ferret and human transcriptome data with *in vivo* analysis using ferrets emphasizes the value of single-cell ferret transcriptome datasets.

RESULTS

Temporal patterns of neurogenesis and gliogenesis in the cerebral cortex of ferrets

First, we confirmed histochemically the spatial and temporal pattern of RG, oRG, and IPC and the appearance of diverse cortical neurons to determine the period in which samples were to be taken for scRNA-seq (**Fig. S1**). While neurogenesis mostly terminated by P5 in the somatosensory area (**Fig. S1A, S1B**), oligodendrocyte progenitors of dorsal origin ($OLIGO2^{+}$) and RG with gliogenic potential ($GFAP^{+}$) became detectable approximately at E40 and increased in number postnatally (**Fig. S1C, S1D**). Based on these observations, we decided to examine single cell transcriptomes at embryonic days E25, E34, and E40 and postnatal days P5 and P10, which recapitulate neurogenesis and gliogenesis.

Single-cell RNA-seq revealed subtypes of cortical cells in ferrets

To identify the temporal trajectories of cell types in the course of ferret brain development (schematically represented in **Fig. 1A**), we performed single-cell RNA-sequencing of ferret somatosensory cortex at the six developmental time points described above (**Fig. 1**). Despite

132 several previous transcriptome studies on the ferret cortex (Johnson et al, 2018; de Juan
133 Romero et al, 2015), information on the ferret genome is incomplete (specifically, poor
134 information regarding the 3′-untranslated region of genes), which has impeded high resolution
135 single-cell transcriptome analyses that can offer an accurate comparison with human datasets.
136 Thus, we first improved the annotations of ferret genomic DNA sequences using Chromium
137 droplet sequencing, which tagged all contigs from a long genomic DNA in a droplet, and
138 constructed new gene models based on the improved genomic annotations (**Table S1, see also**
139 **Materials and Methods**). We performed scRNA-seq using cell populations isolated in two
140 ways to enrich the progenitor subtypes (**Fig. 1A**): (1) FACS-based sorting of the neural stem
141 cell fraction labeled with an AzamiGreen (AG)-driven *HES5* promoter (Ohtsuka et al, 2006)
142 and (2) collecting cells forming the VZ, SVZ, and intermediate zones (IZ) of cerebral cortices
143 after discarding the cortical plate (CP, **Fig. 1B**). We combined these two cell populations on
144 all the sampling stages for unbiased clustering. **Figure 1C** shows cell clustering projected in
145 the Uniform Manifold Approximation and Projection (UMAP) space (preprint: McInnes et al,
146 2018; Stuart et al, 2019). We characterized 26 transcriptionally distinct clusters from 30,234
147 ferret cortical cells through corticogenesis and detected up to 2,600 median genes per cell (**Fig.**
148 **S2A, S2B; Table S1**). Cell clusters were annotated according to their specific gene expression
149 patterns (**Fig. 1D, 1E, S2C, Table S1**) and assigned into ten cell types: RG (early, mid, and
150 late), IPC, OPC, ependymal cells, excitatory cortical neurons (DL and UL), inhibitory neurons
151 (ITN), microglia, endothelial cells, mural cells, and unknown cells (**Fig. 1C**). Early and late
152 RG, and IPC were subdivided into three subclusters that expressed different cell cycle markers
153 (**Fig. S2D**).
154
155 RG, IPC, and neuronal clusters were aligned according to the neuronal differentiation process
156 in the UMAP plot (**Fig. 1C**). RG cells were classified into three clusters (early, mid, and late)
157 according to their collection stages and also the expression of temporally altered RG markers
158 reported previously (hereafter named temporal markers) (Okamoto et al, 2016; Telley *et al*,
159 2019). The "early RG" clusters comprised E25 cells while the "mid RG" clusters, mostly E34
160 cells (**Fig. S2E**).
161
162 Remarkably, we identified a small cluster (409 cells) of *PAX6*-expressing RG subtype, 69% of
163 which expressed *CRYAB* (**Fig. 1F**). *CRYAB*, encoding a molecular chaperone (Yamamoto et
164 al, 2014) is a unique marker for human tRG (Nowakowski et al, 2016); therefore, we designated
165 them as tRG-like cells in ferrets. In contrast, oRG cells failed to be distinguished from

166 ventricular RG cells (vRG) in ferrets by unbiased clustering alone (see below). HOPX, a typical
167 marker for oRG in human tissues (**Fig. 1G, S2F**; Pollen et al, 2015), has been indeed detected
168 in both oRG and vRG at late stages *in vivo* in ferrets (**Fig. S2F**; Johnson et al, 2018; Kawaue
169 et al, 2019).
170
171 **tRG emerge around birth during the development of somatosensory cortex in ferrets**
172 The presence of a tRG-like cluster in ferret transcriptomes led us to investigate the properties
173 of the cells in this cluster. To examine their cell morphology, we sparsely labeled NPC by
174 electroporating P0 embryos with an expression vector for enhanced green fluorescent protein
175 (EGFP) and found a cell population showing major characteristics of human tRG cells
176 (Nowakowski et al, 2016): expression of CRYAB and PAX6 with an apical endfoot and
177 truncated basal fiber in the VZ during late neurogenesis (**Fig. 2A, 2B**). CRYAB expression
178 emerged shortly prior to birth (day 41), gradually increasing in cell number, and became mostly
179 restricted to tRG-shaped cells in the VZ and SVZ (**Fig. 2C, 2D, S3A**). These CRYAB^{+} cells
180 were mostly post-mitotic (KI67^{-}) and neither IPC (TBR2^{+}) nor OPC (OLIG2^{+}) at P10, while a
181 small fraction of those cells expressed these markers at P5 (**Fig. 2F–H**). These histochemical
182 observations were consistent with our single-cell transcriptome data (**Fig. S3B–H**). Altogether,
183 we concluded that tRG-like cells in ferrets are equivalent to human tRG cells (as also confirmed
184 by transcriptomic comparison between humans and ferrets, shown later). A difference in the
185 late neurogenic cortex between humans and ferrets is that the VZ and OSVZ are connected by
186 conventional RG cells in ferrets (Fig. S3A), but separated in humans due to the disappearance
187 of conventional RG cells (Nowakowski et al, 2016).
188
189 **tRG are formed from the apical division of RG sibling cells with a short basal fiber**
190 Continuing with the ferret model, we investigated through time-lapse imaging of cortical slices
191 how tRG are formed (see **Materials and Methods**). We could reconstruct the process of tRG
192 formation from mitotic progenitor cells in four EGFP–labeled lineages. In all cases, vRG cells
193 did not directly differentiate into CRYAB^{+} tRG. In two cases (**Fig. 3A–C**), we could identify
194 a vRG as a grandmother cell of tRG. This vRG produced the mother IPC of tRG, which bore
195 both an apical endfoot and a short basal fiber and underwent interkinetic nuclear migration
196 (**Fig. 3A**). These mother IPC underwent an asymmetric division to generate a non-CRYAB
197 expressing cell and a CRYAB^{+} tRG. Fixed and stained sections are shown in **Fig. 3C**.
198

199 In the other two cases (**Fig. 3D–F**), the mother IPC of tRG also possessed both an apical
200 endfoot and a short basal fiber (**Fig. 3D**) and generated a tRG by asymmetric apical division.
201 The birth of the mother IPC from their parental vRG could not captured because of the onset
202 of time-lapse imaging after the parental vRG division. Altogether, our data suggest that tRG
203 cells are formed by apical asymmetric division(s) from unique apical IPC with a short basal
204 fiber (Tsunekawa et al, in preparation). We note the possibility that these mother IPC, which
205 asymmetrically generated tRG, had already expressed CRYAB. Indeed, some CRYAB-
206 expressing tRG (approximately 20%) were mitotically active but were neonatally silenced (**Fig.
207 2F**).
208

209 **Temporal fates of RG cells are predicted by pseudo-time trajectory analysis**

210 To understand the relationship between various cortical progenitors in the developing ferret
211 brain, particularly in the origin and fate of ferret tRG, pseudo-time trajectory analysis was
212 performed. Single cells that had been subjected to single-cell transcriptome analyses (from E25
213 to P10) were unbiasedly ordered along a trajectory based on their transcriptome profiles (**Fig.
214 S4A, S4B**). To simplify our analysis, we first excluded interneurons, microglia, endothelial
215 cells, and excitatory neuronal clusters. Subsequently, 6,000 single cells were randomly selected
216 from the remaining cell population for further analysis. The pseudo-time analysis predicted a
217 reasonable trajectory consisting of three branching points that generated seven states (**Fig. 4A,
218 S4B**). We assigned major cell types for each state based on the cell clusters defined by UMAP
219 analysis (**Fig. 1C, Table S2**). The trajectory successfully predicted cortical development in the
220 somatosensory area, along which *HES1*$^{+}$ stem cells shift their features from the earlier to the
221 later stages, generating branches of differentiated cells (**Fig. 4B, 4C, S4D**). Major *HES1*$^{+}$stem
222 cell states (state 1, 3, 5 and 7) contained cells at different stages; thus termed NPC1, 2, 3 and
223 astrogenic, respectively (**Fig. S4C**). NPC1 (mostly from E25) bifurcated into the neuronally
224 differentiated lineage and NPC2 state (**Fig. S4B**), which produced the OPC lineage and NPC3
225 state at the second branching point. When neurogenesis gradually declined after birth, the
226 NPC3 state, mainly consisting of late RG cells and tRG (**Fig. S4C**), adopted two states, state 6
227 with an ependymal fate (*FOXJ1*$^{+}$, *SPARCL1*$^{+}$, *AQP4*$^{+}$) and state 7 with astrogenic fate (*FOXJ1*$^{-}$,
228 *SPARCL1*$^{+}$, *AQP4*$^{+}$), as judged by the combination of late fate markers (Liu et al, 2022;
229 Saadoun and Papadopoulos, 2010; Yu et al, 2008, **Fig. 4A, 4D**).
230

231 Remarkably, tRG cell population was distributed into three states along the pseudo-time
232 trajectory (**Fig. 4E, 4F**): NPC3 (mainly during E40–P1), astrogenic (P1–P10), and ependymal
233 (P5–P10) states, suggesting that tRG prenatally arise as precursors of ependyma and astroglia
234 in the ferret cortex.
235
236 **tRG cells possess ependymal and gliogenic potential during cortical development in**
237 **ferrets**
238 To test the hypothesis that tRG generate both ependymal cells and astroglia populations, we
239 first examined the expression of an ependymal marker, FOXJ1, a master regulator of
240 ciliogenesis, according to CRYAB expression in the VZ. We observed that CRYAB^{+} tRG
241 cells gradually co-expressed FOXJ1, reaching up to 90% co-expression by P10 (**Fig. 5A,**
242 **5B**). Similarly, our transcriptome data showed that the fraction of *CRYAB-FOXJ1* double-
243 positive cells increased in the tRG cluster from P1 to P10, whereas other RG clusters
244 maintained low *CRYAB* expression (**Fig. 5C, 5D**). From P5 onwards, differentiating
245 ependymal cells (*CRYAB-FOXJ1* double-positive) accumulated within the VZ (**Fig. 5A**).
246 These cells often align their nuclei in parallel to the ventricular surface, near which nuclear
247 line aggregates are observed more frequently (**Fig. 2B**), and their cell body finally settled on
248 the apical surface with short basal fibers by P14 (**Fig. 5E**). These data indicate that a majority
249 of tRG cells progressively upregulates *FOXJ1* expression to adopt an ependymal cell fate
250 during postnatal development. Concomitantly, adenine cyclase III expression in both
251 primary and multiciliated cells indicated that ciliogenesis progressed postnatally, forming
252 multiciliated ependymal cells on the ventricular surface of the ferret cortex by P35 (**Fig.**
253 **S5A**).
254
255 Moreover, a fraction of tRG belongs to the state 7 (astrogenic state) in the pseudo-time
256 trajectory (**Fig. 4E, 4F**). We examined whether these tRG cells differentiate into astrogenic
257 cells. We chose *FOXJ1* as an ependymal marker and *SPARCL1* as an early astrogenic marker
258 based on a recent study in mice (Liu *et al*, 2022). While *SPARCL1* is expressed in all states
259 generated by NPC2 (**Fig. S5B**), *SPARCL1* expression is highest in astrogenic tRG among the
260 three tRG subgroups, whereas *FOXJ1* expression is nearly exclusive to ependymal tRG (**Fig.**
261 **5F**). Furthermore, cells expressing high levels of *SPARCL1* do not express *FOXJ1* (**Fig. 5G,**
262 **Table S3**). These features of the astrogenic tRG are essentially the same as those of the
263 astrogenic state (state 7) of the pseudo-time trajectory (**Fig. 4D**). Consistently, whereas

264 FOXJ1^{+} cells were located close to the apical surface, those expressing *SPARCL1* were
265 observed relatively far from the apical surface in the VZ (**Fig. 5G, S5C, Table S4**). Altogether,
266 our analyses strongly suggest that tRG cells adopt both the ependymal and astrogenic fates.
267
268 **Ferrets and humans show a homologous developmental transcriptomic profile of**
269 **progenitor subtypes**
270 Both ferrets and humans are positioned in distinct phylogenetic branches; both represent
271 complex brain features of gyrencephalic mammals. Therefore, we compared our temporal
272 series of ferret single-cell transcriptomes with a previously published human dataset
273 (Nowakowski et al, 2017) to examine which processes are species-specific or common for the
274 two species. We merged the two datasets by pairing mutual nearest neighbor cells (MNN)
275 following canonical correlation analysis (CCA) across species (Stuart and Butler et al, 2019)
276 and found that many cell types, including RG, IPC, OPC, and neurons, were clustered together
277 (**Fig. 6A, 6B, S6A**). Transcriptomic trajectories were homologous across the two species,
278 indicating that the transition and differentiation of progenitors are essentially shared by the two
279 species. Nonetheless, the timescales of cortical development significantly differed: on the
280 UMAP plot, ferret E25 cells closely distributed with human GW8 cells; ferret E34, with human
281 GW11–14; ferret E40–P1, with human GW15–16; and ferret P5–P10, with human GW17–22
282 (**Fig. 6B**).
283
284 Next, we compared the similarities among individual RG subtypes across species. To quantify
285 the features of an RG subtype, we introduced the parameter "genescore" (Bhaduri et al, 2020),
286 which reflected the enrichment and specificity of a marker gene for a given cluster (see
287 **Materials and Methods**). Comparison of genescores of two arbitrary RG subtypes between
288 two species revealed a high correlation in the early and late RG clusters (vRG, and oRG for
289 the human dataset) across species (**Fig. 6C, 6D, Table S5**).
290
291 tRG cells also showed a remarkable similarity between the two species (**Fig. 6C, 6D**), as
292 represented by *CRYAB*, *EGR1,* and *CYR61* expression (**Fig. 6E**). To better examine this
293 similarity, we defined the "cluster score" for individual cells as a linear combination of the
294 expression level of marker genes in a cell, which is weighted by its genescore in the human
295 cluster of interest. Calculation of the cluster score for ferret tRG using genescores of the human

296 tRG cluster resulted in a higher score than any other cluster in both datasets (**Fig. 6F**). These
297 results confirm, via transcriptomics, that the ferret tRG cluster is very close to the human one.
298
299 **Transcriptional analysis of human tRG subtypes by integration with ferret tRG subtypes**
300 Next, we assessed whether human tRG cells also possessed ependymal and gliogenic potential,
301 as observed in ferret cells. We chose a recently published human dataset at GW25 (Bhaduri et
302 al, 2021) for comparison because the GW25 dataset includes more tRG cells than the previous
303 datasets. After excluding neurons and other cell types from the analysis, we identified
304 respective human clusters for tRG and oRG cells based on their marker gene expression (**Fig.**
305 **7A, Table S6).** Then, we merged human and ferret NPCs (**Fig. 7B, 7C**) as described before
306 (**Fig. 6A**). This procedure revealed that human tRG and oRG share similar transcriptomes with
307 ferret tRG and later RG, respectively (**Fig. S7A, S7B**). It is worth noting that early RG in ferrets
308 showed the highest similarity with "OLIG1" in human data, and no cell type in human data
309 corresponded to ferret "midRG," likely because only GW25 cells were used for comparison
310 (**Fig. S7B**).
311
312 The integration of ferret and human datasets showed that tRG from both species were mainly
313 distributed into three different clusters: 7, 21, and 28 (**Fig. 7F, S7C**). Cluster 7 cells highly
314 expressed late onset RG genes (such as *APOE*, *FABP7*, *NOTCH2*, and *DBI*; **Fig. S7D**),
315 suggesting that tRG cells in cluster 7 were presumably at a late RG-like state, being not yet
316 committed to neither astrogenic nor ependymal fates (mostly in the NPC 3 state in the ferret
317 pseudo-time trajectory; **Fig 4A, 4E**). In contrast, cells in clusters 21 and 28 highly expressed
318 marker genes for the astrocyte (*GFAP* and *AQP4*), and the ependymal (*FOXJ*1) clusters,
319 respectively (**Fig. S7D, Table S6**). Then, we confirmed that the three states of ferret tRG cells,
320 committed to the astroglia, ependymal fates and uncommitted states, were largely assigned to
321 clusters 21, 28 and 7, respectively (**Fig. 7G**), guaranteeing the reliability of this method. Thus,
322 our results suggested that tRG cells in both humans and ferrets possessed the potential to
323 generate astrocytes and ependymal cells. We note that the proportion of the three types of tRG
324 was different between human and ferret datasets (**Fig. 7D–F**). This may be ascribed to the
325 differences in developmental stages between the two datasets in terms of tRG fate .
326
327 **Prediction of ferret oRG-like cells via the identification of cells homologous to human**
328 **oRG cells**

329 As mentioned before, oRG could not be identified as a separate cluster in the ferret dataset (**Fig.**
330 **1**). We attempted to assign oRG-like cells in the ferret dataset using human oRG cells as
331 anchors via the integration of two datasets by the MNN after CCA (**Fig. 7B**). We could assign
332 oRG-like cells, which were located near the human oRG cluster (**Fig. 7H**). To assess the degree
333 of similarity to human oRG, we calculated the oRG score for each ferret oRG-like cell as we
334 did for tRG (**Fig. 6F**). The assigned oRG-like cells had significantly higher oRG cluster scores
335 than all other NPCs (**Fig. 7I**). Furthermore, we searched genes that were highly expressed in
336 oRG-like cells by comparing oRG-like cells and other NPCs in the ferret dataset (**Table S6**).
337 Consistent with the human dataset (Bhaduri *et al*, 2021), the expression of *HOPX, CLU,* and
338 *CRYM* was higher in oRG-like cells than in other ferret NPCs (**Fig. 7J, S7E**). However, human
339 oRG markers such as *HOPX* and *CLU* were also expressed by vRG and tRG in ferrets (**Fig.**
340 **S2F, S7F**). Therefore, oRG at the transcriptome level can only be distinguished by the whole
341 transcriptome or a combination of several markers, but not by a few marker genes.
342
343 **DISCUSSION**
344 In this study, we made a ferret dataset of single-cell transcriptomes of neural progenitors
345 covering the entire cortical neurogenenesis and early gliogenic phase, revealing their
346 diversity and temporal patterns during cortical development. Comparison of these features
347 between ferrets and humans (Nowakowski *et al*, 2017; Bhaduri *et al*, 2021) indicated at a
348 high resolution that these two gyrencephalic mammals shared a large proportion of
349 progenitor variations and their temporal sequences despite their extremely different
350 neurogenesis timescales. It is remarkable that tRG is conserved between these two
351 phylogenetically distant species. A ferret model easily allowed us to identify the mode of
352 tRG generation and its descendant fates and to analyze cell dynamics in tissues. These
353 findings have not been realized by previous studies on humans, which reexamines the use of
354 ferrets as a valuable model species to study the neural development of gyrencephalic animals.
355
356 **The origin and fates of tRG revealed through live imaging and single cell transcriptomics**
357 Live imaging of ferret brains indicated that tRG form via asymmetric divisions of RG-like
358 progenitors with short radial fibers. In ferrets, this type of progenitors is observed as vRG
359 sibling cells from earlier neurogenic stages (an unpublished observation by Tsunekawa and
360 Matsuzaki). Our observations suggest that these progenitors change from being neurogenic to
361 producing tRG around the boundary of the late neurogenic and early gliogenic stages,

contributing to ependymal formation and gliogenesis. Since the sample size was small, further studies on the process of tRG generation are needed.

We found that ferret (and presumably also human) tRG cells differentiate into ependymal cells and astrogenic cells. This indicates that tRG is a type of intermediate progenitor that generates the terminally differentiated cell type (ependymal cells) and astrogenic progenitors. This mode of ependymal cell formation is likely parallel to that of the bifurcation of ependymal cells and adult neural stem cells from the same progenitor population in the striatum on the ventral side (Ortiz-Álvarez *et al*, 2019).

Our intensive cross-species analysis on tRG classified human tRG into three classes that corresponded to the three subtypes of ferret tRG (**Fig. 7E**). Unlike in ferret brains, the uncommitted tRG fraction is dominant in GW25 human brains, suggesting that human tRG at GW25 progresses along the differentiation axis less than ferret tRG at P5–P10, most of which are already committed to either ependymal or astrogenic states. GW25 is almost at the latest stages experimentally available in human brains due to ethical reasons. However, ferret tRG significantly resemble human tRG not only in morphology and transcriptomes, but also in the presence of the minor human tRG populations of the ependymal and gliogenic states. Human tRG are highly likely to differentiate into both ependymal and astrogenic cells, which later populate the white matter. Here, our cross-species analysis highlights the notable role of tRG as progenitors contributing to the formation of the ependyma and white matter, both of which are critical for cortical expansion in gyrencephalic mammals.

MATERIALS AND METHODS

EXPERIMENTAL MODEL AND SUBJECT DETAILS

Ferret brain tissue samples

Pregnant ferrets were purchased from Marshall BioResources. We also bred them to maintain a population that is sufficient to regularly get pregnant females in the animal facility of RIKEN Center for Bioisystems Dynamics Reseach under the license given from Marshall BioResources. All procedures during animal experiments were performed in accordance with the legal and institutional ethical regulations of RIKEN Center for Biosystems Dynamics Research.

395 Ferret pups are born at day 41 or day 42 of gestation. The day of birth was counted as postnatal
396 day 0 (P0). Ferret embryos and pups were euthanized prior to brain removal.
397 Samples used for single cell RNA-sequencing were obtained from 1 or 2 pups for each
398 developmental stage: embryonic days 25, 34 and 40 and postnatal days 1, 5 and 10. Samples
399 used for immunohistology-based quantifications were obtained from 2 or 3 pups from different
400 mothers. Samples used for a time-lapse imaging were obtained from 1 animal per experiment,
401 which is performed 4 times, independently.
402
403 **METHOD DETAILS**
404 **Genome assembly and gene model construction of the ferret genome**
405 RNA-seq library preparation and sequencing
406 Total RNA was extracted from the embryonic tissues (Supplementary Table S7) using the
407 RNeasy mini kit (Qiagen). Concentration and length distribution of the RNA were checked
408 with the Qubit RNA HS Assay Kit on a Qubit 2.0 Fluorometer (Thermo Fisher Scientific) and
409 the RNA 6000 Nano Kit on a 2100 Bioanalyzer (Agilent Technologies). Sequencing libraries
410 were prepared using 1 μg of total RNA with the TruSeq Stranded mRNA Sample Prep Kit
411 (Illumina) and the TruSeq single-index adaptor (Illumina), except for the sample 'gonad and
412 mesonephros' (see Supplementary Table S7) for which 500 ng of total RNA was used. The
413 RNA was fragmented at 94°C for either 8 minutes or 2 minutes, which resulted in libraries
414 with variable insert size distributions (Hara *et al*, 2015). The optimal numbers of PCR cycles
415 were pre-determined using the KAPA Real-Time Library Amplification Kit (Roche) as
416 described previously (Tanegashima *et al*, 2018). Libraries were sequenced with the Rapid Run
417 mode of HiSeq1500 (Illumina) using the HiSeq PE Rapid Cluster Kit ver. 2 (Illumina) and the
418 HiSeq Rapid SBS Kit v2-HS (Illumina) to produce paired-end reads of 127 nucleotides. Base
419 calling was performed with RTA ver. 1.18.64, and the fastq files were generated with bcl2fastq
420 ver. 1.8.4 (Illumina).
421
422 Genomic DNA extraction and Chromium genome library construction
423 Genomic DNA was extracted from a liver of an adult female ferret using the CHEF Mammalian
424 Genomic DNA Plug Kit (BioRad, Cat. No. #1703591). In brief, the liver tissue of about 50 mg
425 was homogenized in PBS (-) with a Dounce tissue grinder on ice, fixed with ethanol, and
426 subsequently embedded in low melting point agarose gel (BioRad). After the protein digestion
427 with Proteinase K (QIAGEN, Cat. No. #158920) and RNA digestion with RNase A (QIAGEN,
428 Cat. No. #158924), the gel plugs were further digested by Agarase (Life Technologies, Cat.

429 No. #EO0461). DNA was purified by the drop dialysis method using the MF-Millipore
430 Membrane Filter (Merck Millipore, Cat. No. #VCWP04700). Length distribution of the
431 genomic DNA was analyzed by pulsed-field gel electrophoresis, which exhibited an average
432 length of over 2 Mbp. The Chromium library was constructed using the Chromium Genome
433 Reagent Kit v1 Chemistry (10x Genomics, Cat No. #PN-120216), and sequencing was
434 performed with an Illumina HiSeq X to obtain paired-end 151 nt-long reads.
435
436 Genome assembly
437 De novo genome assembly using the Chromium linked-reads was performed with Supernova
438 ver. 2.0.0 (10x Genomics) with the default parameters, and the resultant sequences were output
439 with the option 'pseudohap'. Detection and masking of repetitive sequences were performed
440 using RepeatMasker ver. 4.0.7 (Smit et al, 2013-2015) with NCBI RMBlast ver. 2.6.0+ and the
441 species-specific repeat library from RepBase ver. 23.01.
442
443 Gene model construction
444 Gene models for gene expression level quantification were constructed in the three following
445 steps. First, ab initio gene prediction was performed by BRAKER ver. 2.0.5 (Hoff *et al*, 2019).
446 In this process, GeneMark-ET ver. 4.33 (Lomsadze *et al*, 2014) with the information of spliced
447 RNA-seq alignment was used for training, and AUGUSTUS ver. 3.3 (Stanke *et al*, 2008) with
448 the parameters of `UTR=on, species=human` was used for gene prediction. For the
449 abovementioned training of BRAKER, the RNA-seq reads were aligned to the repeat-masked
450 genome sequences by STAR ver. 2.5.4a (Dobin *et al*, 2013) with default parameters using the
451 entire set of RNA-seq reads of various tissue types (Supplementary Table S7). Second, the
452 information of RNA-seq alignment was directly incorporated into the gene models to improve
453 the coverage of the 3' UTR region of each gene which is not reliably predicted in ab initio gene
454 prediction. This computation was performed with HISAT2 ver. 2.1.0 (Kim *et al*, 2019) and
455 StringTie ver. 1.3.4d (Kovaka *et al*, 2019), whose output GTF file was merged with the gene
456 models produced by BRAKER using the merge function of StringTie. Finally, the existing
457 transcript sequences of MusPutFur1.0 available at NCBI RefSeq (GCF_000215625.1) was
458 incorporated into the gene models by mapping their sequences to the repeat-masked genome
459 sequences using GMAP ver. 2017-11-15 (Wu & Watanabe, 2005) with the `not report chimeric
460 alignments` option. The gene name of each locus was adopted from the annotation in RefSeq,
461 and the gene name of a newly predicted locus was assigned according to the results of a
462 BLASTX search against the UniProtKB Swiss-Prot database release 2020_01. The assignment

463 was performed only for genes with a bit score (in the abovementioned BLASTX search) of
464 greater than 60. When a locus has multiple transcripts, the one with the highest score was
465 adopted for gene naming. If a transcript estimated by ab initio prediction bridged multiple
466 genes, they were incorporated into the gene models as separate genes.
467
468 Completeness assessment of assemblies
469 To assess the continuity of the genome assembly and gene space completeness of the gene
470 models, gVolante ver. 1.2.1 (Nishimura *et al*, 2017) was used with the CEGMA ortholog search
471 pipeline and the reference orthologues gene set CVG (Hara *et al*, 2015).
472
473 ***In utero* and postnatal electroporation**
474 *In utero* electroporation (IUE) and postnatal electroporation in ferrets was performed as
475 described previously (Kawasaki *et al*, 2012; Matsui *et al*, 2013; Tsunekawa *et al*, 2016 for IUE;
476 Borrell, 2010 for postnatal electroporation) with modifications. Briefly, pregnant ferrets or
477 ferret pups were anesthetized with isoflurane at indicated stages of the development. The
478 location of lateral ventricles was visualized with transmitted light delivered through an optical
479 fiber cable. Three µl of plasmid DNA solution was injected into the lateral ventricle at indicated
480 developmental stages using an injector. Each embryo or pup was placed between the paddles
481 of electrodes, and was applied a voltage pulse of 45V at the duration from 100 msec to 900
482 msec (100,0 Pon and 1000,0 Poff) 10 times for in utero electroporation, and under the same
483 condition except a voltage of 60V for postnatal electroporation (CUY21 electroporator, Nepa
484 Gene).
485
486 **Plasmids**
487 To assure a stabilized expression of transgenes, we combined expression vectors with a
488 hyperactive piggyBac transposase system to integrate expression vectors into the genome for
489 a stable expression (Yusa *et al*, 2011). To enrich neural progenitor cell populations in "AG"
490 samples used for the single-cell transcriptome analysis, pLR5-Hes5-d2-AzamiGreen (0.5
491 µg/µl; Hes5 promoter was gifted from Kageyama Laboratory; Ohtsuka *et al*, 2006) was
492 electroporated at E30 for E40, or at E34 for postnatal samples, together with pCAX-hyPBase
493 (0.5 µg/µl). Among them, for P1 and P10 samples, pPB-LR5-mCherry (0.5 µg/µl) was also
494 included in the DNA solution.
495 To sparsely label the cell cytoplasm for detailed imaging of individual cells on vibratome-cut
496 thick cortical sections, we have used pPB-LR5-floxstop-EGFP (0.5 µg/µl) combined with a

497 low concentration of Cre-expressing plasmid (pCAG-Cre, 1 ng/μl). For all IUE experiments,
498 Fast Green solution (0.1 mg/ml; Wako Pure Chemical Industries) was added into the freshly
499 prepared mixture of plasmid DNA to visualize the injection.
500 For in situ hybridization probes, the PCR product was inserted into pCR-BluntII-TOPO for
501 cloning and sequencing.
502
503 **Library preparation for scRNAseq**
504 10x v2 Chromium was performed on dissociated single cells according to the manufacturer's
505 protocol.
506
507 **Single cell isolation and sorting of Azamigreen-expressing cells**
508 Cell suspension was prepared as reported previously (Wu *et al*, 2022) with modifications.
509 Brains were collected at indicated stages, transferred in the ice-cold dissection Dulbecco's
510 Modified Eagle Medium (DMEM) F12 and meninges were removed. Somatosensory area was
511 dissected from embryonic or postnatal cortices using an ophthalmic knife (15°) under a
512 dissection microscope. Sliced tissues were dissociated via enzymatic digestion with papain at
513 37°C for 30 - 45 min in ice-cold Hank's Balanced Salt Solution (HBSS) (-) with EDTA (0.1
514 M). Dissociated cells were centrifuged at 1000xg for 5 min to remove papain by washing with
515 PBS and were resuspended in 0.375% BSA/HBSS (-), or in the sorting buffer (DMEM F12 +
516 GlutamaX (Thermo Fisher); 0.1 % of Penicillin/Streptomycin (Millipore); 20 ng/ml human
517 basic FGF, Peprotech; 1xB27 RA-, Gibco) for cell sorting (see below). Homogenous cell
518 suspension filtered through 35 μm strainer (Falcon).
519 To concentrate neural progenitor cell (NPC) populations at the expense of mature neurons, two
520 methods were used for each sample, except for E25, from which cells were collected using
521 whole somatosensory area:
522 1) "T" samples: the cortical plate (CP) of cortical sections were dissected out and a part of the
523 intermediate zone (IZ) was likely to be included in the discarded region.
524 2) "AG" samples: brains collected at indicated stages were electroporated in utero by
525 azamiGreen (AG)-expression vector under the control of Hes5 promoter. The latter method
526 allows the expression of AG in only NPC by the presence of a degradation signal "d2" in the
527 vector to degrade AG protein in HES5-negative differentiating progeny. Only "AG" samples
528 were processed with cell sorting and dissociated cell obtained as described above were placed
529 in a SH800 cell sorter (SONY) to sort azamigreen-positive cells in 0.375%BSA/HBSS(-)

530 solution. Cell survival and cell number were quantified by Countess or Countess II (Invitrogen),
531 prior to an application of single cell isolation using 10x v2 Chromium kit.
532 Samples from the same developmental stage, except for P10 "T" sample, were born from the
533 same mother and were collected by applying either of above methods on the same day and
534 processed in parallel.
535
536 Library preparation and Sequencing
537 Single-cell libraries were generated according to the manufacturer's instructions. Cell
538 suspensions were diluted for an appropriate concentration to obtain 3,000 cells per channel of
539 a 10X microfluidic chip device and were then loaded on the 10X Chromium chips accordingly
540 to the manufacturer's instructions.
541 Total cDNA integrity and quality were assessed with Agilent 2100 Bioanalyzer.
542 Libraries were sequenced on the HiSeq PE Rapid Cluster Kit v2 (Illumina), or the TruSeq PE
543 Cluster Kit v3-cBot-HS, to obtain paired-end 26 nt (Read 1)-98 nt (Read 2) reads.
544
545 **Cortical slice culture for a time-lapse imaging**
546 Brain slices were prepared as previously described (Shitamukai *et al*, 2011). Briefly, coronal
547 slices were prepared from E38 ferret embryos or P0 pups, and embedded in 4% low-melting
548 agarose (UltraPure LMP agarose, Thermo Fischer Scientific) before sectioning with a
549 vibratome (LinerSlicer, DOSAKA EM, 450 μm). Floating sections were collected and washed
550 in DMEM/F-12 on ice. For time-lapse imaging, slices were mounted on a filter insert (Millicell
551 from Millipore) with collagen type Ia. Slices were then incubated in DMEM/F-12 culture
552 medium containing 1X B-27 (RA-) and N2 supplements, and 1% penicillin-streptomycin-
553 glutamine (without serum) at 37°C with 5% of CO2 supply, for 1 or 2 hours prior to the live-
554 imaging in the same culture solution. Slices were maintained for 3 days in culture and the
555 medium was changed every other day.
556
557 **Time-lapse imaging**
558 To follow the process of tRG formation, we electroporated E35 embryonic brains with an
559 EGFP-expressing vector and performed time-lapse imaging of cortical slices in culture from
560 E38 or P0 for three days, based on the first appearance of tRG (**Fig. 2C**). Imaging was
561 performed by two-photon microscopes (A1R MP+, Nikon) equipped with a 16X objective lens
562 (CFI 75 LWD 16XW, Nikon), a MaiTai excitation laser (Spectra Physics) and an incubation
563 chamber supplied with 5% CO2, 40% O2 and 55% N2. 890 nm of wavelengths was used for

564 exciting EGFP. Images were taken by 7 μm z-stacks at every 20 min. ND acquisition images
565 were analyzed and reconstructed by using MetaMorph (Molecular Devices, USA). These slices
566 were fixed right after the end of imaging, and immunostained for CRYAB and EGFP to find
567 division sequences generating tRG.
568
569 **Immunostaining of brain slices after time-lapse imaging and observations**
570 Brain slices after a live imaging were fixed for 1 overnight in 1% paraformaldehyde (PFA) in
571 0.1M phosphate buffer (PB, pH 7.4) at 4°C, and coronal sections with 12μm thickness were
572 made as described in the following section, and were incubated overnight at 4°C with chicken
573 anti-EGFP antibody (Aves lab, USA) and mouse anti-CRYAB monoclonal antibody (Abcam,
574 UK) at 1/1000 dilution in the blocking solution. Fluorescent images were acquired from the
575 cryostat sections under an FV1000 confocal microscope (Olympus, Japan) and reconstructed
576 by using Volocity software (PerkinElmar, USA).
577
578 **Immunohistology and confocal imaging**
579 Ferret brains were removed from embryos or pups and fixed for 1 or 2 overnights, respectively,
580 in 1% paraformaldehyde (PFA) prepared in 0.1M phosphate buffer (PB, pH 7.4) at 4°C. P35
581 ferrets were transcardially perfused with cold PBS, followed by 4% PFA, under deep
582 anesthesia with isoflurane, then collected brains were post-fixed with 1% PFA. After the
583 fixation of brains or cortical tissue slices after a live imaging, they were equilibrated in 25%
584 sucrose overnight before embedding in O.C.T. compound (TissueTek, Sakura) and frozen in
585 liquid nitrogen. Frozen samples were stored at -80°C prior to a coronal sectioning using a
586 cryostat (CM3050S Leica Microsystems, 12μm sections). After equilibration at room
587 temperature, sections were washed in PBS with 0.1% Tween (PBST), followed by a treatment
588 with an antigen retrieval solution of HistoVT one (Nacalai Tesque) diluted 10 times in milliQ
589 water, at 70°C for 20 min. Sections were then blocked 1 hr at the room temperature (RT) in
590 PBS with 2% Triton-X100 and 2% normal donkey serum (Sigma), followed by an incubation
591 overnight at 4°C with primary antibody diluted in the blocking solution. After washing in PBST
592 three times, sections were treated with appropriate fluorescence-conjugated secondary
593 antibodies (1:500) along with 4',6-diamidino-2-phenylindole (DAPI, 1:1,000) for 1 hr at room
594 temperature. Sections were washed again prior to mounting with PermaFluor solution (Therma
595 Fisher Scientific).
596 Immunostaining of thick ferret brain sections (200 μm) were performed as previously reported
597 (Tsunekawa et al., 2016). Briefly, ferret brains were fixed in 1%PFA, washed in PB overnight

598 at 4°C, and embedded in 4% low-melting agarose (UltraPure LMP agarose, Thermo Fischer
599 Scientific). Embedded brains were sliced coronally at 200 μm thickness by a vibratome
600 (LinerSlicer, DOSAKA EM) on ice. Floating sections were washed three times with PBST,
601 treated with the blocking solution for 1 hour at RT and incubated with primary antibodies for
602 5 or 6 overnights at 4°C under shaking. Sections were then washed in PBST and treated with
603 secondary antibodies for 5 or 6 overnights at 4°C under shaking. After washing, we mounted
604 brain slices with CUBIC solution 2 to allow the transparency.
605 Fluorescent images were acquired using an FV1000 confocal microscope (Olympus, Japan).
606 Somatosensory cortices were captured with 20X or 100X objective lenses. When 100x
607 objective lens was used, z-stacks of confocal images were taken with an optical slice thickness
608 1.0 μm or 1.5 μm and MAX-projection images obtained by FiJi are shown.
609 All the antibodies used in this study are listed in Key Resources Table, and are used at
610 following concentrations: chicken anti-EGFP, 1:500; mouse anti-Alpha B Crystallin, 1:500;
611 Rabbit anti-FoxJ1, 1:500; goat anti-Olig2, 1:500; rat anti-Eomes, 1:500; rabbit anti-Pax6,
612 1:500; mouse anti-Pax6, 1:500; mouse anti Gfap, 1:500; rabbit anti-HopX, 1:500; rat anti-RFP,
613 1:500; goat anti-adenine cyclase III, 1:250; rat anti-Ctip2, 1:500; mouse anti-Satb2, 1:500, rat
614 anti-Ki67, 1:500.
615
616 **Probe preparation**
617 Primers for PCR targeting ferret *CLU* gene were designed with Primer3 ver 0.4.0 software.
618 Total RNA was isolated from embryonic ferret brain, collected in Trizol. cDNA was generated
619 from total RNA using the Prime Script 1st strand cDNA synthesis kit (Takara) according to the
620 manufacturer's recommended procedure. Target cDNA was inserted into pCR-TOPOII-Blunt
621 plasmid for cloning and sequencing using M13F or M13R primers. Anti-sense cRNA probes
622 were then generated by in vitro transcription using T7 promoter.
623
624 ***In situ* hybridization**
625 ISH was performed as described previously, with some modifications (Mashiko *et al*, 2012).
626 Briefly, ferret brains were perfused in 4%PFA in PBS and were fixed at 4%PFA in 0.1M PB,
627 Fixed brain were incubated in 30% sucrose/4%PFA in 0.1M PB for at least 1 day and were
628 stored at -80℃ until ISH. Frozen brains were sectioned in coronal plane at 25 μm using cryostat
629 (CM3050S Leica Microsystems). Sections on slides were post-fixed at 4% PFA in 0.1M PB
630 and treated with proteinase K (Roche). Sections were hybridized with digoxigenin (DIG)-

631 labeled probes at 72° C overnight in hybridization solution. Sections were then washed and
632 blocked with donkey serum and incubated with pre-absorbed DIG antibody, conjugated to
633 Alkaline phosphatase for 2 hours at room temperature. Color development was performed in
634 solution containing NBT/BCIP (Roche).
635
636 ***In situ* hybridization with RNAscope**
637 To detect mRNA of ferret Sparcl1, RNAscope multiplex fluorescent detection reagents v2 was
638 used with Sparcl1 probe (Advanced cell diagnostics). In situ hybridization was performed
639 according to the manufacturer's instructions. After that sections were block with 3%
640 milk/PBST and stained with antibody of FOXJ1.
641
642 **QUANTIFICATION AND STATISTICAL ANALYSIS FOR scRNAseq.**
643
644 Statistical details including experimental n, statistical tests and significance are reported in
645 Figure Legends.
646
647 **Alignment and raw processing of data**
648 Fastq files were obtained from individual samples and were processed using Cell Ranger
649 pipeline v2. Alignment was done using "Cell Ranger count" function with default parameters
650 accordingly to manufacturer's instructions to map reads to the ferret reference (MPF_Kobe
651 2.0.27) or NCBI database (NCBI Assembly ID: 286418 (MusPutFur1.0)). The raw data for
652 each set of cells within a sample was obtained by cellranger count function and was read using
653 Seurat "Read10X" function (Seurat v3.1.5) (Stuart *et al*, 2019), creating a matrix for unique
654 molecular identified (UMI) counts of each gene within each cell. Detailed information after
655 mapping is listed in the Supplementary Table S1B.
656
657 **Filtering and normalization**
658 Filtering and normalization were performed using Seurat (v3.1.5) (Stuart *et al*, 2019). Briefly,
659 each sample was filtered by removing low-quality cells with unique feature counts less than
660 200, and genes expressed in less than 3 cells (Seurat function "CreateSeuratObject"). Different
661 samples were then merged using the Seurat "merge" function. Merged data was further subset
662 by keeping cells with features (genes) over 200 and less than 5000. Raw UMI counts were then
663 normalized using "LogNormalize" as normalization method, which divided reads by the total

number of UMIs per cell, then multiplied by 10,000 (Seurat "NormalizeData" function). This resulted in a total of 30,234 cells and 19,492 genes: E25 (3486 cells), E34AG (3223 cells), E34T (2260 cells), E40AG (1102), E40T (1581 cells), P1AG (2681), P1T (3641), P5AG (2429), P5T (2926), P10AG (3010) and P10T (3895).

Single-cell clustering and visualization

Cell clustering was employed to the entire cell population after removing low-quality cells, using Seurat (v3.1.5) (Stuart *et al*, 2019). 2,000 highly variable genes were identified and used for the downstream analysis using Seurat "FindVariableFeatures" function (selection.method = "vst"), which allowed the calculation of average expression and dispersion for each gene. Normalized data was then processed for scaling using Seurat function "Scale Data" with default settings, which also allowed the regression of the batch. Principal component analysis (PCA) was performed with 2,000 variable genes to reduce dimensionality of the scaled dataset and 50 PCs were retained (Seurat "RunPCA" function). Clustering was then performed using graph-based clustering approach ("Find Neighbors" function) using top 20 PCs, which were selected based on the standard deviation of PCs on the elbowplot created by Seurat function "ElbowPlot" and based on statistical significance calculated by JackStraw application. Briefly, cells are embedded in a k-nearest neighbor (KNN) graph based on the Euclidean distance in a PCA space. Then, this knn graph is used to group cells on a shared nearest neighbor graph based on calculations of overlap between cells with similar gene expression patterns (Jaccard similarity). Cells were then clustered by Louvain algorithm implemented in Seurat "ClusterCells" function (resolution = 0.8, dims = 1:20). Next, we used Seurat "RunUMAP" function, which resulted in cell clusters being separated in embedding space while preserving the balance between local and global structure.

Cluster annotations

Cluster markers were obtained using "FindAllMarkers" Seurat function. We tested genes that showed at least a 0.25-fold difference between the cells in the cluster and all remaining cells, and that were detected in more than 25% of the cells in the cluster. Clusters, which we called subtypes, were then annotated by comparing cluster markers to previously identified cell type markers in the literature for mouse and human datasets. The full list of markers is given under Table S1. The heatmap in Figure 2D shows the expression data for the top 10 highly expressed marker genes for each cluster using a downsampling of maximum 500 cells from each cluster. Plotting cells onto the UMAP plot by their batch indicated that batches did not influence

clustering (**Fig. 2C**) in accordance with the differential expression of cluster markers (Figure 2D, S2C). When a cluster was enriched based on the developmental stage, the information was included in the annotation. For example, "early RG" cluster was enriched in E25 samples, and expressed both common radial glial cell markers shared with other RG clusters in our dataset, but also expressed early onset-genes reported in mouse studies (Okamoto *et al*, 2016; Telley *et al*, 2019), such as *HMGA2*, *FLRT3*, *LRRN1* (Table S1). Therefore, we named this cluster as "early RG" based on its age-dependent properties.

To achieve more precise clustering, cycling cells were identified with known markers implemented in Seurat package (S genes and G2M genes). Clusters enriched in S genes or G2M genes were identified, including early_RG2 (S), early_RG3 (G2M), late_RG2 (G2M), late_RG3 (S), IPC2 (S) and IPC3 (G2M) (Figure S2B). Subtypes of RG and IPC clusters were further combined to facilitate the data representation (Figure S2C-D).

Differential gene expression analysis

Differential gene expression (DEG) analysis was assessed using "FindMarkers" Seurat function with default parameters.

Pseudotime analysis

Monocle 2 was used to construct developmental trajectories based on pseudotime ordering of single cells (Qiu *et al*, 2017; Trapnell *et al*, 2014). We generated a subset of clusters using "SubsetData" Seurat function using the raw counts. Combined progenitor clusters (F_earlyRG, F_midRG, F_lateRG, F_tRG, F_IPC, F_OPC) were selected. All clusters known to be generated from a non-cortical origin including microglia, endothelial and mural cells, were removed prior the pseudotime analysis. The expression matrix and a metadata file that contained above cluster information defined by Seurat were used as input for monocle package (Table S2).

The "differentialGeneTest" function was used to select genes for dimensionality reduction (fullModelFormulaStr = '~Subtype.combined'). Top 1,000 genes were then applied for cell ordering. The visualization of the minimum spanning tree on cells was obtained by Monocle2 "plot_complex_cell_trajectory" function. To visualize the ordered cells on Seurat's UMAP plot, we extracted the branch information for cells and added as metadata of the merged Seurat object ("AddMetaData" Seurat function).

Processing External scRNA-seq Datasets for comparisons and preprocessing

732 scRNA-seq data of developing human brain from Nowakowski *et al*. (2017) and from Bhaduri
733 *et al*. (2021) were used. All cells included in the analysis and cluster assignments from the
734 provided matrix were mapped to the cell type assignments provided in the metadata of
735 Nowakowski et al. dataset and the cell type labels were used as provided by the authors without
736 modification. For Bhaduri et al. dataset, GW25 sample was used for clustering by Seurat
737 package as described above. For both, we removed low quality cells and clusters annotated
738 based on anatomical regions other than somatosensory cortex, and removed cells with less than
739 200 features. For Bhaduri et al. dataset, we filtered to cells with at least 200 features, less than
740 6,500 features and less than 5% mitochondrial genes. This resulted in 25,485 cells from around
741 180,000 cells in Bhaduri et al. dataset, and in 2,673 cells in Nowakowski et al. dataset.
742
743 **Integrated analysis of human and ferret scRNA-seq datasets**
744 Human datasets published by Bhaduri *et al*. (2021) and Nowakowski *et al*. (2017) were used
745 for integration analysis with our ferret dataset using Seurat canonical correlation analysis
746 (Stuart *et al*, 2019). First, a Seurat object was created for all datasets as described previously.
747 Briefly, each object was individually processed with a normalization and variable features were
748 identified. For human datasets, we excluded cells or samples obtained from anatomical regions
749 other than somatosensory cortex. Then, the integration anchors between human and ferret
750 Seurat objects were identified using "FindIntegrationAnchors" Seurat function with default
751 settings. The integration was then performed with "IntegrateData" Seurat function. Scaling,
752 PCA and UMAP dimensional reduction were performed to visualize the integration results.
753
754 **Cluster correlation analysis between ferret and human clusters.**
755 Correlation analysis was performed as described by Bhaduri *et al*. (2020), with modifications.
756 Briefly, lists of cluster marker genes obtained by "FindAllMarkers" Seurat function on
757 individual datasets were extracted prior to an integration (Table S5A), except for Nowakowski
758 et al dataset, for which the marker gene list was provided. A score based on the specificity and
759 the enrichment of cluster marker genes was generated (defined as "Genescore"). A genescore
760 value was obtained by the multiplication of the average fold change that represents the gene
761 enrichment, with the percentage of the cells expressing the marker in the cluster (pct.1) divided
762 the percentage of the cells from other clusters expressing the marker (pct.2: specificity). This
763 function was employed on the marker genes for a human subtype of interest in the space of
764 marker genes for ferret NPC (RG, IPC, OPC and EP) clusters. Genescores for both ferret and
765 human were then obtained for all markers shared between human subtype of interest (i.e. oRG)

766 and ferret NPC subtypes. We then applied cor.test function using Pearson method to estimate
767 a correlation and the significance of the correlation for the obtained genescores between ferret
768 and human samples. These resulting values were represented for NPC subtypes on heatmap
769 plots.
770
771 **Prediction of oRG-like/tRG-like cells by cross-dataset analysis.**
772 The cell type marker genes for oRG and tRG cell types were extracted from each human
773 scRNAseq datasets. To predict human oRG-like and tRG-like cells in ferret sample more
774 precisely, we removed mature neuron, microglia, and endothelia clusters, as well as clusters
775 assigned as unknown, from individual datasets for an integration between ferret and human
776 NPC clusters using Seurat package as described in the above section (Stuart *et al*, 2019). After
777 identification of anchors between human and ferret Seurat objects using
778 "FindIntegrationAnchors", we extracted the information of each pair of anchors, which
779 including one ferret and one human cell. If the human cell in the pair belongs to oRG (tRG)
780 cluster in human dataset, we consider the other ferret cell in the same pair as oRG (tRG)-like
781 cell.
782
783 **Cluster score calculation.**
784 Based on a genescore calculated for marker genes as previously described, a cell-type
785 predictive model was generated. For both datasets, our custom-made R scripts were applied to
786 generate matrices using either human oRG markers or tRG markers using our integrated
787 subsets. In the space of matrices reduced with corresponding human marker genes, a score we
788 defined as "oRG score" or "tRG score" was created by multiplying human genescore for each
789 marker genes with the expression values of these genes in all cells present in the integrated
790 subset data. The results were represented by beeswarm and boxplot.
791
792 **Evaluation of immunolabeled cell number and statistical analysis**
793 The counting frames on images of immunolabeled sections consisted of 150 μm of width
794 regions of interests (ROIs). The numbers of immunolabeled cells within selected ROIs were
795 manually counted using the "cell counter" tool of FiJi software (Schindelin *et al*, 2012). The
796 VZ was identified by its cell density visualized by DAPI, and according to its thickness
797 measured by a vertical length from the ventricular surface at indicated stages (100 μm at P5,
798 70 μm at P10). The proportions of immunolabeled cells positive for various markers were

799 calculated using the summed data counted within all ROIs. The data obtained from lateral
800 cortices of somatosensory area was averaged from 2 to 3 sections.
801 For CRYAB-positive cells, we only counted cells with nuclei which were visualized by DAPI
802 staining. The numbers of positive cells were counted using two or three different animals.
803 Quantification was followed by Wilcoxon test to assess statistical significance and data on each
804 section were considered as n = 1.
805
806 **Quantification of RNAscope in situ hybridization and immunostaining image**
807 Images of RNAscope in situ hybridization and FOXJ1 immunostaining were captured by using
808 an IX83 inverted microscope (Olympus) equipped with Dragonfly 200 confocal unit (Andor),
809 Zyla Z4.2 sCMOS camera (Andor), and UPLXAPO 60XO objective lens (Olympus). Imaging
810 was performed to satisfy Nyquist sampling (xy = 48 nm/pixel by using 2x zoom optic and z =
811 136 nm interval) and 3D deconvolution was performed by ClearView-GPU™ option of Fusion
812 software (Andor). Default deconvolution parameter is used except for number of irritation (n
813 = 24) and mounting media reflection index (RI = 1.46). For quantification of images,
814 CellProfiler version 4.2.4 (Stirling *et al*, 2021) was used. To detect mRNA dots of RNAscope
815 in situ hybridization images, a single Z section of deconvolved images were processed by
816 EnhancingSpeckles module (10 pixels size) and then mRNA dots were detected by
817 IdentifyPrimaryObjects module, adaptive Otsu two class method, using default parameter
818 except for size of adaptive window (size = 10). Dot's diameter less than 4 pixels were removed
819 as a background noise. Cytoplasmic ROIs were generated from smoothed RNAscope in situ
820 hybridization images by MedianFilter module (window size = 10) and manually drawn seed
821 ROIs of DAPI staining images by using IdentifySecondaryObjects module (propagation
822 adaptive Otsu two class method, using default parameter). FoxJ1 immunostaining raw images
823 were measured by MeasureImageIntensity module. Quantified data were visualized and
824 clustered by using RStudio (version 2022.07.1+554) with R (version 4.0.3). Each of mRNA
825 count data and protein staining intensity data was log transformed and normalized, and
826 hierarchical clustering was done by using a Euclidian distance and complete clustering method
827 and cut tree to 4 clusters. Each cluster expression was plotted and classified to single or double
828 positive, or double negative of SPARCL1 and FOXJ1 populations.
829
830 **Data and code availability**
831 Genome assembly and chromium linked-read sequences were deposited in the DDBJ under
832 accession numbers BLXN01000001–BLXN01022349 and DRA010274. The gene models are

available from Figshare under the DOI: 10.6084/m9.figshare.12807032. Single-cell RNA-seq data have been deposited in the DDBJ under the number PSUB013536.

Any information required to obtain and reanalyze the data reported in this paper is available from the lead contact upon request.

Acknowledgements

We thank Kazuaki Yamaguchi, Rohab F. Abdelhamid, and Chiharu Tanegashima for sequencing RNA and genomic DNA and all members of the Laboratory of Cell Asymmetry for providing technical support and helpful discussions. This work was supported by JSPS KAKENHI [Grant Numbers 18H04003, 17H05779, 19H04791] and RIKEN. RIKEN funds F.M. M.B. was a RIKEN International Program Associate. Q.W. was supported by a JSPS Postdoctoral Fellowship and a RIKEN Special Postdoctoral Researcher Program.

Author contributions

M.B., Q.W., and F.M. designed experiments. M.K., O.N., Q.W., Y.K., and S.K. constructed new ferret gene models. M.B. and Q.W. performed scRNA-seq experiments and bioinformatics analyses. M.B., Y.T., and Q.W. performed molecular biological analyses. M.B., T.S. [Taeko] and T.S. [Tomomi] performed histological analyses. A.S and Q.W. performed and analyzed RNA/protein double-tissue staining. T.S. [Taeko] carried out time-lapse imaging. T.S. [Taeko], Y.T. and H.K. bred the ferrets. M.B., Q.W., A.S. and F.M. wrote the manuscript. All authors read and approved the final manuscript for submission.

Competing interests statement

The authors declare no competing interests.

References

Bhaduri A, Andrews MG, Mancia Leon W, Jung D, Shin D, Allen D, Jung D, Schmunk G, Haeussler M, Salma J, *et al* (2020) Cell stress in cortical organoids impairs molecular subtype specification. *Nature* 578(7793): 142–148

Bhaduri A, Sandoval-Espinosa C, Otero-Garcia M, Oh I, Yin R, Eze UC, Nowakowski TJ & Kriegstein AR (2021) An atlas of cortical arealization identifies dynamic molecular signatures. *Nature* 598(7879): 200–204

Borrell V (2010) In vivo gene delivery to the postnatal ferret cerebral cortex by DNA

electroporation. *J Neurosci Methods* 186: 186–195
Capecchi MR & Pozner A (2015) ASPM regulates symmetric stem cell division by tuning Cyclin E ubiquitination. *Nat Commun* 6:8763
Chen EY, Tan CM, Kou Y, Duan Q, Wang Z, Meirelles G V., Clark NR & Ma'ayan A (2013) Enrichr: interactive and collaborative HTML5 gene list enrichment analysis tool. *BMC Bioinformatics* 14
deAzevedo LC, Fallet C, Moura-Neto V, Daumas-Duport C, Hedin-Pereira C & Lent R (2003) Cortical radial glial cells in human fetuses: Depth-correlated transformation into astrocytes. *J Neurobiol* 55(3): 288–298
Dobin A, Davis CA, Schlesinger F, Drenkow J, Zaleski C, Jha S, Batut P, Chaisson M & Gingeras TR (2013) STAR: ultrafast universal RNA-seq aligner. *Bioinformatics* 29: 15–21
Fietz SA, Kelava I, Vogt J, Wilsch-Bräuninger M, Stenzel D, Fish JL, Corbeil D, Riehn A, Distler W, Nitsch R, *et al* (2010) OSVZ progenitors of human and ferret neocortex are epithelial-like and expand by integrin signaling. *Nat Neurosci* 13(6): 690–699
Fujimori A, Itoh K, Goto S, Hirakawa H, Wang B, Kokubo T, Kito S, Tsukamoto S & Fushiki S (2014) Disruption of Aspm causes microcephaly with abnormal neuronal differentiation. *Brain Dev* 36(8): 661–669
Hansen D V., Lui JH, Parker PRL & Kriegstein AR (2010) Neurogenic radial glia in the outer subventricular zone of human neocortex. *Nature* 464(7288): 554–561
Hara Y, Tatsumi K, Yoshida M, Kajikawa E, Kiyonari H & Kuraku S (2015) Optimizing and benchmarking de novo transcriptome sequencing: From library preparation to assembly evaluation. *BMC Genomics* 16: 1–12
Hoff KJ, Lomsadze A, Borodovsky M & Stanke M (2019) Whole-Genome Annotation with BRAKER. *Methods Mol Biol* 1962: 65–95
Huang W, Bhaduri A, Velmeshev D, Wang S, Wang L, Rottkamp CA, Alvarez-Buylla A, Rowitch DH & Kriegstein AR (2020) Origins and Proliferative States of Human Oligodendrocyte Precursor Cells. *Cell* 182(3): 594-608.e11
Jayaraman D, Kodani A, Gonzalez DM, Mancias JD, Mochida GH, Vagnoni C, Johnson J, Krogan N, Harper JW, Reiter JF, *et al* (2016) Microcephaly Proteins Wdr62 and Aspm Define a Mother Centriole Complex Regulating Centriole Biogenesis, Apical Complex, and Cell Fate. *Neuron* 92(4): 813–828
Johnson MB, Sun X, Kodani A, Borges-Monroy R, Girskis KM, Ryu SC, Wang PP, Patel K, Gonzalez DiM, Woo YM, *et al* (2018) Aspm knockout ferret reveals an evolutionary mechanism governing cerebral cortical size. *Nat 2018 5567701* 556: 370–375
Johnson MB, Wang PP, Atabay KD, Murphy EA, Doan RN, Hecht JL & Walsh CA (2015) Single-cell analysis reveals transcriptional heterogeneity of neural progenitors in human cortex. *Nat Neurosci* 18(5): 637–646
de Juan Romero C, Bruder C, Tomasello U, Sanz-Anquela JM & Borrell V (2015) Discrete domains of gene expression in germinal layers distinguish the development of gyrencephaly. *EMBO J* 34(14): 1859–1874
Kawasaki H, Iwai L & Tanno K (2012) Rapid and efficient genetic manipulation of gyrencephalic carnivores using in utero electroporation. *Mol Brain* 5:24
Kawaue T, Shitamukai A, Nagasaka A, Tsunekawa Y, Shinoda T, Saito K, Terada R, Bilgic M, Miyata T, Matsuzaki F, *et al* (2019) Lzts1 controls both neuronal delamination and outer radial glial-like cell generation during mammalian cerebral development. *Nat Commun* 10(1): 2780
Kessaris N, Fogarty M, Iannarelli P, Grist M, Wegner M & Richardson WD (2006) Competing waves of oligodendrocytes in the forebrain and postnatal elimination of an embryonic lineage. *Nat Neurosci 2005 92* 9: 173–179

919 Kim D, Paggi JM, Park C, Bennett C & Salzberg SL (2019) Graph-based genome alignment
920 and genotyping with HISAT2 and HISAT-genotype. *Nat Biotechnol 2019 378* 37: 907–
921 915
922 Kou Z, Wu Q, Kou X, Yin C, Wang H, Zuo Z, Zhuo Y, Chen A, Gao S & Wang X (2015)
923 CRISPR/Cas9-mediated genome engineering of the ferret. *Cell Res* 25(12): 1372–1375
924 Kovaka S, Zimin A V., Pertea GM, Razaghi R, Salzberg SL & Pertea M (2019)
925 Transcriptome assembly from long-read RNA-seq alignments with StringTie2. *Genome*
926 *Biol* 20: 1–13
927 Kuleshov M V., Jones MR, Rouillard AD, Fernandez NF, Duan Q, Wang Z, Koplev S,
928 Jenkins SL, Jagodnik KM, Lachmann A, *et al* (2016) Enrichr: a comprehensive gene set
929 enrichment analysis web server 2016 update. *Nucleic Acids Res* 44: W90–W97
930 Liu J, Liu W, Yang L, Wu Q, Zhang H, Fang A, Li L, Xu X, Sun L, Zhang J, *et al* (2017) The
931 Primate-Specific Gene TMEM14B Marks Outer Radial Glia Cells and Promotes
932 Cortical Expansion and Folding. *Cell Stem Cell* 21(5): 635-649.e8
933 Liu J, Wu X & Lu Q (2022) Molecular divergence of mammalian astrocyte progenitor cells
934 at early gliogenesis. *Development* 149(5): dev199985
935 Lomsadze A, Burns PD & Borodovsky M (2014) Integration of mapped RNA-Seq reads into
936 automatic training of eukaryotic gene finding algorithm. *Nucleic Acids Res* 42
937 Mashiko H, Yoshida AC, Kikuchi SS, Niimi K, Takahashi E, Aruga J, Okano H & Shimogori
938 T (2012) Comparative Anatomy of Marmoset and Mouse Cortex from Genomic
939 Expression. *J Neurosci* 32: 5039–5053
940 Matsui A, May T, C. YA, S. KS, Mami U, Masaharu O & Tomomi S (2013) BTBD3
941 Controls Dendrite Orientation Toward Active Axons in Mammalian Neocortex. *Science*
942 342(6162): 1114–1118
943 McInnes L, Healy J & Melville J (2018) UMAP: Uniform Manifold Approximation and
944 Projection for Dimension Reduction. *arXiv* doi: 1802.03426v3 [PREPRINT]
945 Nishimura O, Hara Y & Kuraku S (2017) gVolante for standardizing completeness
946 assessment of genome and transcriptome assemblies. *Bioinformatics* 33: 3635–3637
947 Nowakowski TJ, Bhaduri A, Pollen AA, Alvarado B, Mostajo-Radji MA, Di Lullo E,
948 Haeussler M, Sandoval-Espinosa C, Liu SJ, Velmeshev D, *et al* (2017) Spatiotemporal
949 gene expression trajectories reveal developmental hierarchies of the human cortex.
950 *Science* 358(6368): 1318–1323
951 Nowakowski TJ, Pollen AA, Sandoval-Espinosa C & Kriegstein AR (2016) Transformation
952 of the Radial Glia Scaffold Demarcates Two Stages of Human Cerebral Cortex
953 Development. *Neuron* 91(6): 1219–1227
954 Ohtsuka T, Imayoshi I, Shimojo H, Nishi E, Kageyama R & McConnell SK (2006)
955 Visualization of embryonic neural stem cells using Hes promoters in transgenic mice.
956 *Mol Cell Neurosci* 31(1): 109–122
957 Okamoto M, Miyata T, Konno D, Ueda HR, Kasukawa T, Hashimoto M, Matsuzaki F &
958 Kawaguchi A (2016) Cell-cycle-independent transitions in temporal identity of
959 mammalian neural progenitor cells. *Nat Commun* 7: 11349
960 Ortiz-Álvarez G, Daclin M, Shihavuddin A, Lansade P, Fortoul A, Faucourt M, Clavreul S,
961 Lalioti ME, Taraviras S, Hippenmeyer S, *et al* (2019) Adult Neural Stem Cells and
962 Multiciliated Ependymal Cells Share a Common Lineage Regulated by the Geminin
963 Family Members. *Neuron* 102(1): 159-172.e7
964 Polioudakis D, de la Torre-Ubieta L, Langerman J, Elkins AG, Shi X, Stein JL, Vuong CK,
965 Nichterwitz S, Gevorgian M, Opland CK, *et al* (2019) A Single-Cell Transcriptomic
966 Atlas of Human Neocortical Development during Mid-gestation. *Neuron* 103(5): 785-
967 801.e8
968 Pollen AA, Nowakowski TJ, Chen J, Retallack H, Sandoval-Espinosa C, Nicholas CR, Shuga

969 J, Liu SJ, Oldham MC, Diaz A, *et al* (2015) Molecular Identity of Human Outer Radial
970 Glia during Cortical Development. *Cell* 163(1): 55–67
971 Pulvers JN, Bryk J, Fish JL, Wilsch-Bräuninger M, Arai Y, Schreier D, Naumann R, Helppi
972 J, Habermann B, Vogt J, *et al* (2010) Mutations in mouse Aspm (abnormal spindle-like
973 microcephaly associated) cause not only microcephaly but also major defects in the
974 germline. *Proc Natl Acad Sci U S A* 107(38): 16595–16600
975 Qiu X, Mao Q, Tang Y, Wang L, Chawla R, Pliner HA & Trapnell C (2017) Reversed graph
976 embedding resolves complex single-cell trajectories. *Nat Methods* 14(10): 979–982
977 Rash BG, Duque A, Morozov YM, Arellano JI, Micali N & Rakic P (2019) Gliogenesis in
978 the outer subventricular zone promotes enlargement and gyrification of the primate
979 cerebrum. *Proc Natl Acad Sci* 116(14): 7089 LP – 7094
980 Reillo I & Borrell V (2012) Germinal Zones in the Developing Cerebral Cortex of Ferret:
981 Ontogeny, Cell Cycle Kinetics, and Diversity of Progenitors. *Cereb Cortex* 22: 2039–
982 2054
983 Rowitch DH & Kriegstein AR (2010) Developmental genetics of vertebrate glial–cell
984 specification. *Nature* 468(7321): 214–222
985 Saadoun S & Papadopoulos MC (2010) Aquaporin-4 in brain and spinal cord oedema.
986 *Neuroscience* 168(4): 1036–1046
987 Schindelin J, Arganda-Carreras I, Frise E, Kaynig V, Longair M, Pietzsch T, Preibisch S,
988 Rueden C, Saalfeld S, Schmid B, *et al* (2012) Fiji: an open-source platform for
989 biological-image analysis. *Nat Methods 2012 97* 9: 676–682
990 Shitamukai A, Konno D & Matsuzaki F (2011) Oblique radial glial divisions in the
991 developing mouse neocortex induce self-renewing progenitors outside the germinal zone
992 that resemble primate outer subventricular zone progenitors. *J Neurosci* 31: 3683–3695
993 Sidman RL & Rakic P (1973) Neuronal migration, with special reference to developing
994 human brain: a review. *Brain Res* 62(1): 1–35
995 Smart IHM, Dehay C, Giroud P, Berland M & Kennedy H (2002) Unique Morphological
996 Features of the Proliferative Zones and Postmitotic Compartments of the Neural
997 Epithelium Giving Rise to Striate and Extrastriate Cortex in the Monkey. *Cereb Cortex*
998 12(1): 37–53
999 Stanke M, Diekhans M, Baertsch R & Haussler D (2008) Using native and syntenically
1000 mapped cDNA alignments to improve de novo gene finding. *Bioinformatics* 24: 637–
1001 644
1002 Stirling DR, Swain-Bowden MJ, Lucas AM, Carpenter AE, Cimini BA & Goodman A
1003 (2021) CellProfiler 4: improvements in speed, utility and usability. *BMC Bioinformatics*
1004 22
1005 Stuart T, Butler A, Hoffman P, Hafemeister C, Papalexi E, Mauck WM, Hao Y, Stoeckius M,
1006 Smibert P & Satija R (2019) Comprehensive Integration of Single-Cell Data. *Cell*
1007 177(7): 1888-1902.e21
1008 Tanegashima C, Nishimura O, Motone F, Tatsumi K, Kadota M & Kuraku S (2018)
1009 Embryonic transcriptome sequencing of the ocellate spot skate Okamejei kenojei. *Sci*
1010 *Data 2018 51* 5: 1–6
1011 Telley L, Agirman G, Prados J, Amberg N, Fièvre S, Oberst P, Bartolini G, Vitali I, Cadilhac
1012 C, Hippenmeyer S, *et al* (2019) Temporal patterning of apical progenitors and their
1013 daughter neurons in the developing neocortex. *Science* 364
1014 Trapnell C, Cacchiarelli D, Grimsby J, Pokharel P, Li S, Morse M, Lennon NJ, Livak KJ,
1015 Mikkelsen TS & Rinn JL (2014) The dynamics and regulators of cell fate decisions are
1016 revealed by pseudotemporal ordering of single cells. *Nat Biotechnol* 32(4): 381–386
1017 Tsunekawa Y, Terhune RK, Fujita I, Shitamukai A, Suetsugu T & Matsuzaki F (2016)
1018 Developing a de novo targeted knock-in method based on in utero electroporation into

1019 the mammalian brain. *Development* 143(17): 3216–3222
1020 Wu Q, Shichino Y, Abe T, Suetsugu T, Omori A, Kiyonari H, Iwasaki S & Matsuzaki F
1021 (2022) Selective translation of epigenetic modifiers affects the temporal pattern and
1022 differentiation of neural stem cells. *Nat Commun 2022 131* 13: 1–18
1023 Wu TD & Watanabe CK (2005) GMAP: a genomic mapping and alignment program for
1024 mRNA and EST sequences. *Bioinformatics* 21: 1859–1875
1025 Yamamoto S, Yamashita A, Arakaki N, Nemoto H & Yamazaki T (2014) Prevention of
1026 aberrant protein aggregation by anchoring the molecular chaperone αB-crystallin to the
1027 endoplasmic reticulum. *Biochem Biophys Res Commun* 455: 241–245
1028 Yu X, Ng CP, Habacher H & Roy S (2008) Foxj1 transcription factors are master regulators
1029 of the motile ciliogenic program. *Nat Genet* 40(12): 1445–1453
1030 Yusa K, Zhou L, Li MA, Bradley A & Craig NL (2011) A hyperactive piggyBac transposase
1031 for mammalian applications. *Proc Natl Acad Sci U S A* 108: 1531–1536
1032 Zheng K, Wang C, Yang J, Huang H, Zhao X, Zhang Z & Qiu M (2018) Molecular and
1033 Genetic Evidence for the PDGFRα-Independent Population of Oligodendrocyte
1034 Progenitor Cells in the Developing Mouse Brain. *J Neurosci* 38: 9505–9513
1035 Zhong S, Zhang S, Fan X, Wu Q, Yan L, Dong J, Zhang H, Li L, Sun L, Pan N, *et al* (2018)
1036 A single-cell RNA-seq survey of the developmental landscape of the human prefrontal
1037 cortex. *Nature* 555(7697): 524–528
1038 Smit, AFA, Hubley, R & Green, P. (2013-2015) *RepeatMasker Open-4.0*. Available at:
1039 http://www.repeatmasker.org.

1040 **FIGURE LEGENDS**

1041

1042 **Figure 1 - Single-cell RNA-seq reveals ferret transcriptome signatures and the cell types.**
1043 **A** Schematic representing cortical development and emergence of diverse neural progenitors
1044 in humans and ferrets. Progenitors sequentially generate DL- and subsequent UL-neurons, and
1045 finally glial cells, and form ependymal cells. RG and oRG have been morphologically and
1046 positionally identified in both humans and ferrets while tRG have been only reported in humans.
1047 VZ, ventricular zone; ISVZ, inner subventricular zone; OSVZ, outer subventricular zone; IZ,
1048 intermediate zone; DL, deep layer; UL, upper layer; CP, cortical plate; NEP cell,
1049 neuroepithelial cell; Mn, migrating neuron; and EP cell, ependymal cell.
1050 **B** Schematic representing the experimental design and time points used to build the
1051 transcriptome atlas of developing somatosensory cortex of ferrets. Single cells were isolated
1052 using 10X Chromium (see Materials and Methods).
1053 **C** UMAP visualization showing cells colored by Seurat clusters and annotated by cell types
1054 (as shown in **C, D**).
1055 **D** Heatmap showing expression profiles of cluster marker genes based on log fold-change
1056 values. Cells were grouped by Seurat clustering (transverse). Cell types were assigned
1057 according to the expression of marker and differentially expressed genes in each cluster. Early
1058 RG was defined by the expression of *HMGA2, LDHA,* and *LIX1*; and late RG, by *PTN, ALDOC,*
1059 and *FABP7*. OPC, oligodendrocyte precursor cell; ITN, interneuron; and EN, endothelial cells.
1060 Other cell type abbreviations are shown in (A) and the main text. Color bar matches the Seurat
1061 clusters in (**C**). The ten most enriched representative genes in each cluster are shown, with
1062 typical marker genes noted in (**E**–**G**).
1063 **E** Normalized expression levels of representative marker genes of different cell types projected
1064 onto the UMAP plot in (**C**). MG, microglia.
1065 **F** Expression pattern of *CRYAB*, a marker for tRG, only described in humans and other primates.
1066 G The expression pattern of *HOPX*, a marker for oRG in humans and other primates in the
1067 UMAP plot.

1068

1069 **Figure 2 - Truncated tRG emerges during postnatal cortical development in ferrets.**
1070 **A** Representative images showing the cellular features of tRG in the ferret at P0, VZ stained
1071 for GFP (red) and CRYAB (green). Ferret embryonic RG were sparsely labelled with a GFP-
1072 expressing plasmid at E30 via IUE. MAX projection was performed on a 30 μm vibratome
1073 section with 5 μm interval for each z-image. Scale bar, 50 μm.

1074 **B** Expression patterns of CRYAB (green) and PAX6 (red) in ferret germinal zones during
1075 postnatal development (P1, P5, and P10) (cryosection thickness = 12 μm).
1076 **C** Developmental profile of CRYAB expression in ferret cortices. Immunostaining for CRYAB
1077 (green) and DAPI (gray) on cryosections at E32, E38, P3, P5, and P10 (cryosection thickness
1078 = 12 μm).
1079 **D** Quantification of $CRYAB^+$ cells among all nuclei (DAPI) in VZ strips through
1080 immunostaining, indicating a great increase in CRYAB-expressing cells (strip width = 150 μm;
1081 n = 3 for P5; n = 2 for P10; Wilcoxon rank-sum test *p*-value = 6.574e-08).
1082 **E–G** Expression of other markers in $CRYAB^+$ cells. Representative images are shown with
1083 MAX projection. Below each double staining image, quantification of KI67-, TBR2-, or
1084 OLIG2-expressing cells among the $CRYAB^+$ cell population in the VZ is shown (n = 2 for P5;
1085 n = 2 for P10 for each staining except n = 3 for TBR2 staining). Box and whisker plots indicate
1086 ranges (lines) and upper and lower quartiles (box) with the median.
1087
1088 **Figure 3 - Generation of ferret tRG by asymmetric division.**
1089 **A–C** Time-lapse imaging of an EGFP-labeled vRG cell, which produced a parental IPC that
1090 asymmetrically divided into tRG (see also the time-lapse movie 1). (**A**) Sequential snapshots.
1091 The time below each snapshot strip indicates the time (hour) passed after the slice culture was
1092 started. The white arrowheads indicate ancestral vRG (pink). The vRG generated an IPC (white
1093 arrows and blue cell body) at 8:00, which underwent an interkinetic nuclear migration (8:00–
1094 48:00), and generated a $CRYAB^+$ daughter (blue) by an asymmetric division (48:00). Open
1095 arrows indicate the other daughter (light blue) of the IPC. (**B**) Schematic of the time-lapse
1096 imaging in (**A**). Colors represent cells as in (**A**). (**C**) The cultured slice was fixed at 84:00 and
1097 stained for EGFP (green), CRYAB (red), and FOXJ1 (light blue). EGFP staining shows that
1098 FOXJ1+cell has a short basal fiber. Scale bar, 50 μm.
1099 **D–F** Time-lapse imaging of an EGFP-labeled IPC forming a tRG. An apically attached IPC
1100 (white arrows, blue cell body) with a short basal fiber produced a tRG cell (blue). (**D**)
1101 Sequential snapshots showing that an IPC formed tRG through apical division at 13:20 as in
1102 (**A**, **B**). tRG sibling cells are marked by light blue color and open arrows. (**E**) Schematic
1103 representation of tRG formation recorded in (**D**). Cells are marked by the same colors as in (**D**).
1104 (**F**) Immunostaining of a cryostat section from a fixed slice stained for CRYAB (red) and EGFP
1105 (green).
1106

1107 **Figure 4 - Temporal fates of RG cells predicted by pseudo-time trajectory analysis.**
1108 **A** Pseudo-time trajectory tree of progenitor cells in the ferret developing cortex (assembled
1109 with Monocle v2). Cellular distribution at each state is the same as in the UMAP plot shown
1110 in Fig. 1C. Cell types representing each state and their gene markers are shown next to each
1111 state (see below).
1112 **B** Trajectory trees split by collection stages (AG samples are shown).
1113 **C** Distribution of cells expressing marker genes for stem cell states (*HES1* and *HMGA2*) and
1114 the neurogenic state (*EOMES*) along trajectories. Color densities indicate the log-normalized
1115 unique molecular identifier count for each gene.
1116 **D** Normalized expression of four genes: *SPARCL1, AQP4, CRYAB,* and *FOXJ1* in the state 6
1117 and state 7 cells in the pseudotime trajectory tree (Fig. 4A). The combination of expression
1118 levels of the four markers gene discriminates state 6 (ependymal) and state 7 astrogenic. See
1119 the text for details.
1120 **E** Distribution of tRG cells along the tree and tRG-focused UMAP visualization. The tRG cells
1121 (n = 162) were found on the three states, NPC3 (9.3%; 15 cells), ependymal-tRG (61.1%; 99
1122 cells), and astrogenic-tRG (29.6%; 48 cells).
1123 **F** Composition of the three types of tRG in (D) by the collection stage (AG and T samples are
1124 combined). No tRG cells were collected from E25 and E34.
1125
1126 **Figure 5 - tRG adopt both ependymal cells and** astrogenic **fates in ferrets.**
1127 **A** Immunostaining of 12 µm cortical cryosections with CRYAB (green) and FOXJ1 (red),
1128 focusing on the VZ at E40, P3, P5, P10, P14, and P35. Scale bar, 50 µm.
1129 **B** Percentage of FOXJ1 expression in CRYAB-expressing cells (n = 3 for P5; n = 2 for P10;
1130 Wilcoxon rank sum test *p*-value = 1.749e-05).
1131 **C** Number of cells expressing both *CRYAB* and *FOXJ1* in the mid and late RG, or tRG clusters
1132 shown in Fig. 1C (with unique molecular identifier counts higher than 0.25). Colored bars
1133 indicate the stages of sample collection. *CRYAB*- and *FOXJ1*-expressing cells increased over
1134 time only in the tRG cluster.
1135 **D** Normalized expression levels of *FOXJ1* in each cell in the indicated ferret clusters in Fig.
1136 1C.
1137 **E** Cortical origin and shape of FOXJ1-expressing ependymal cells indicated with white arrows.
1138 Staining for FOXJ1 at P14 after labeling cortical progenitors with an mCherry-expressing

1139 vector via IUE at E30. The maximum projection images with 1 μm z-step size are shown.
1140 Cryosection thickness = 12 μm; scale bar = 20 μm.
1141 **F** Normalized expression of *SPARCL1* and *FOXJ1* in each cell in ferret tRG clusters separated
1142 by the pseudo-time trajectory analysis (see Table S3).
1143 **G** Relationship between *SPARCL1* and *FOXJ1* transcripts in individual cells within each tRG
1144 cluster. Within the 15 cells that were classified in state 5 tRG, only one expressed *FOXJ1*
1145 mRNA. **Statistics?**
1146 **H** Immunostaining of a P10 cortical tissue for FOXJ1 protein and S*PARCL1* mRNA.
1147 **I** Cells within the VZ in (**H**) were clustered into four classes by FOXJ1 protein± and S*PARCL1*
1148 mRNA±. Cluster A: S*PARCL1*/FOXJ1-/-, B: S*PARCL1*/FOXJ1 +/-, C: S*PARCL1*/FOXJ1-/+,
1149 D: S*PARCL1*/ FOXJ1 +/+ (Fig. S5C, S5D, Table S4). See **Materials and Methods** for
1150 clustering. Scale bar = 20 μm.
1151
1152 **Figure 6 − Comparison of molecular identity of RG subtypes between ferret and human.**
1153 **A** UMAP visualization of integrated human (n = 2,672; left) and ferret (n=30,234; right) single-
1154 cell datasets colored according to the different clusters. The names of clusters from human and
1155 ferret cells begin with "H" and "F," respectively.
1156 **B** Homologous temporal pattern of transcriptomic characters of progenitors and their progenies
1157 between ferrets and humans. Corresponding neurogenic stages between ferrets and humans can
1158 be assigned by cell distribution at homologous positions in UMAP plots. Gliogenic RG cells
1159 (a subtype of the "late_RG" group and OPC in Figure 1**B**) were first distinguished
1160 transcriptionally at ferret E40 and at human GW14, as pointed out by arrows.
1161 **C, D** Correlation coefficient (**C**) and significance (**D**) between indicated clusters of ferrets and
1162 humans, calculated by marker gene scores.
1163 **E** Normalized expression levels of the indicated genes in humans and ferrets from each
1164 progenitor cluster.
1165 **F** tRG scores of the indicated clusters are presented as box and whisker plots for humans and
1166 ferrets. These represent the range without outliers (lines) and upper and lower quartiles with
1167 the median (box). Outliers are represented as points outside the box. Outliers are 1.5-fold larger
1168 or smaller than interquartile range from the third or first quartile, respectively.
1169
1170 **Figure 7 - Identification of tRG subtypes in humans and oRG in ferrets.**

A UMAP visualization of human brain cells colored by cell type and identified by marker genes (data from Bhaduri et al, 2021).

B Schematic of the integration strategy of human and ferret subtypes.

C UMAP visualization of integrated ferret and human datasets colored by different clusters.

D, E Identification of three tRG subtypes in ferrets (D) and humans (E). The red dots highlight the indicated tRG subtypes named after pseudotime trajectory analysis in Fig. 4.

F Distribution of humans (left) and ferrets (right) tRG in the integrated dataset. Human and ferret tRG were identified from the separated dataset.

G Distribution of ferret tRG subtypes (identified by the pseudo-time analysis) in the integrated dataset.

H Identification of oRG-like cells in ferret (left) and oRG cells in human (right), all highlighted as red dots.

I oRG scores for oRG-like cells and other NPCs in ferrets. Box and whisker plots indicate ranges (lines) and upper and lower quartiles with the median (box).

J The expression levels of *CRYM*, *CLU*, and *HOPX* in oRG-like cells and other NPCs in ferrets.

1187 **Supplementary Figure Legends**

1188

1189 **Figure S1 - Temporal pattern of neurogenesis and gliogenesis in the cerebral cortex of**
1190 **ferrets.**

1191 **A** Coronal sections of the somatosensory cortices immunostained for RG (PAX6, red), IPC
1192 (TBR2, green), and OPC (OLIG2, cyan) from early to late neurogenesis at E25, E32, E36, E40,
1193 P5, and P10. Scale bars = 100 µm. The position of the image strip at each stage is shown in the
1194 corresponding dorsal hemisphere image above the strip.

1195 **B** Immunostaining for CTIP2 (green) and SATB2 (red) at the same developmental stages as in
1196 (**A**), showing the onset of DL- (E25 or earlier) and UL-neurogenesis (E32–E34). Scale bars =
1197 100 µm.

1198 **C** Immunostaining for GFAP, a marker showing gliogenic potential, in cortical germinal layers
1199 at E32, E36, E40, P5, and P10. Gliogenic progenitors emerge around E40, while mature
1200 astrocytes with a typical astrocytic morphology appear later at approximately P10 onward in
1201 the outside of the germinal layers (Reillo & Borrell, 2012).

1202 D, E mCherry labeling of the dorsal cortex at E30 showing that a population of OLIG2^{+}
1203 oligodendrocyte precursors are generated in the cerebral cortex by P10.

1204 **E** As reported for both mice and humans (Zheng *et al*, 2018; Rash *et al*, 2019; Huang *et al*,
1205 2020; Kessaris *et al*, 2006). Arrowheads in the cropped images of the left panels (E area in Fig.
1206 S1**D**) indicate cells that co-express mCherry, PAX6, and OLIG2 in the OSVZ. Scale bars = 20
1207 µm.

1208

1209 **Figure S2 - Cell types in developing ferret cerebral cortex.**

1210 **A** Violin plots showing the number of genes and mRNAs per cell in each sample and time
1211 point.

1212 **B** Table comparing quality-control metrics of an alignment with either MusPutFur 1.0 (UCSC
1213 gene models) or MusPutFur 2.60 (this study) using E34 samples. The total number of genes
1214 detected and median genes per cell were higher with MusPutFur 2.60.

1215 **C** Dotplot showing average expression and percentage of expression of representative marker
1216 genes for individual cell types in the merged dataset. The largest cluster was composed of UL
1217 neurons, and their four clusters (Fig. 1**C**) were combined as a single "UL" group. P.E.,
1218 percentage of expressing cells per cell type; A.E., average expression per cell type.

1219 **D** Heatmap showing the expression level of cell cycle marker genes based on log fold-change
1220 values. *PCNA*, *DUT*, *SIVA1,* and *TYMS* are markers of the S-phase; *UBE2C*, *CDCA4*, *CENPF,*

1221 and *CCNB1* are markers of the G2M-phase. Three subclusters among early RG, late RG, and
1222 IPC clusters expressed different markers for cell-cycle states. The color bar at the top indicates
1223 Seurat clusters matching those in Fig. 1**C**.
1224 **E** Percentage of each cell type in the merged dataset (bottom half) and percentage of each stage
1225 of collection in a cell type (top half).
1226 **F** Immunostaining for CRYAB$^+$ tRG (green) and HOPX$^+$ RG (red) together with DAPI on P1
1227 and P10 germinal layers.
1228
1229 **Figure S3 - Development of ferret tRG during postnatal cortical development.**
1230 **A** Cellular features of a tRG cell in cortex labelled with GFP at embryonic stages via IUE.
1231 Vibratome sections at P0 and P4 (thickness = 200 μm) were immunostained for CRYAB
1232 (green) and GFP (red). CRYAB$^+$ truncated basal fibers spanned up to the SVZ.
1233 **B** Pie charts showing the percentage of *CRYAB* expression in the ferret clusters of the merged
1234 transcriptome dataset of all stages (Fig. 1). Cells were counted as positive if unique molecular
1235 identifier counts for *CRYAB* were > 1 using Seurat "WhichCells" function (slot = "counts").
1236 C Number of cells in the tRG clustered by age annotated in the ferret transcriptome dataset
1237 (Fig. 1).
1238 **D** Number of *CRYAB*-expressing cells in RG clusters of the transcriptome dataset (Fig. 1).
1239 *CRYAB* expression was undetectable at E25. *CRYAB*-expressing cells in the midRG and lateRG
1240 subtypes did not change in all stages (cell numbers: 58, 46, 68, 55, and 61 at E34, E40, P1, P5,
1241 and P10, respectively), while the number of *CRYAB*$^+$ tRG cells increased after birth (cell
1242 numbers: 0, 21, 50, 91, and 118 at E34, E40, P1, P5, and P10, respectively).
1243 **E–G** Violin plots indicating the normalized expression of *CRYAB* (**E**), *TBR2* or *EOMES* (**F**),
1244 and *OLIG2* (**G**) in the ferret clusters shown in Fig. 1.
1245
1246 **Figure S4 - Temporal fates of RG cells identified by pseudo-time trajectory analysis**
1247 **A** Ferret cells used for pseudo-time trajectory analysis were lined up along the stretched
1248 pseudo-time axis. Expression levels of markers for typical cell types are also shown along the
1249 pseudo-time axis: *LIX1* and *HMGA2* for early RG, *EOMES* and *NEUROG2* for IP, *RGS20*, and
1250 *PTN* for late RG, *PDGFR* and *OLIG2* for glial cells, and *FOXJ1* and *FAM216B* for ependymal
1251 cells.
1252 **B** Branching trees labelled by pseudo-time score. Color scale indicates log10 (pseudo-time
1253 +0.1) values. Each state is named after the major cell type.

1254 **C** The composition of each state is shown by clusters defined in the UMAP plot (Fig. 1).
1255 Percentages for clusters were calculated from all cells in each state.
1256 **D** Branching trees split by UMAP clusters (Fig. 1).
1257
1258 **Figure S5 - Ferret tRG adopt both ependymal and astrogenic fates in ferrets**
1259 **A** Onset of ciliogenesis in the developing cortex of ferrets, shown via staining for ADENINE
1260 CYCLASE III (cyan) along the VZ surface at E40, P5, P10, and P35. Scale bars = 10 μm.
1261 **B** Normalized expression of *SPARCL1*/cell in the major cell types shown in Fig. 1**C**.
1262 **C** Plots showing *SPARCL1* mRNA count (left) and normalized FOXJ1 protein levels (right) in
1263 each cell clustered into individual classes (**A–D**) within the VZ shown in Fig. 5**H** (Table S4).
1264 The box and whisker plots indicate the range (lines) and the upper and lower quartiles with the
1265 median (box). **Statistics?**
1266 D Distances of each cell (its center of gravity) from the apical surface in the individual clusters
1267 (**A–D**), as indicated by the box and whisker plots in (**C**). **Statistics?**
1268
1269 **Figure S6 - Comparison of molecular identity of RG subtypes between ferret and human**
1270 **A** UMAP visualization of integrated ferret (n = 30,234) and human (n = 2,672) single-cell
1271 datasets colored according to the different clusters. The names of clusters from human and
1272 ferret cells begin with "H" and "F," respectively.
1273 **B** Expression patterns of the indicated genes in each cluster. Circle color indicates the
1274 expression level of each gene. Circles size indicates the percentage of cells expressing the gene
1275 in the indicated cluster.
1276
1277 **Figure S7 - Comparison of the tRG and oRG subtypes between ferrets and humans**
1278 **A, B** Matrices of correlations between two arbitrary RG subtypes from humans and ferrets by
1279 calculating marker gene scores as described for Fig. 6. (**A**) Correlations and (**B**) *p*-values
1280 between pairs in human and ferret clusters are shown. The early RG in ferrets showed the
1281 highest similarity with “OLIG1” in human data. This might be because of two reasons; (1) we
1282 included human cells from GW25 only and no human early RG in this dataset, and (2) cells in
1283 “OLIG1” highly expressed genes related with cell proliferation, as the early RG also did (Table
1284 S6). We did not observe any cell types in human data corresponding to the ferret “midRG”
1285 with the same reason described above.

1286 **C** Distribution of human and ferret tRGs in the integrated dataset. The number in the X-axis
1287 indicates the cluster number identified by the UMAP in Fig. 7C.
1288 **D** Expression pattern of the subtype maker genes in the three tRG-enriched clusters (7, 21, and
1289 28).
1290 **E** Expression patterns of *CRYM*, *CLU*, and *HOPX* in oRG cells and other NPCs in humans.
1291 **F** *In situ* hybridization of *CLU* at the ferret cortex showed its expression in all VZ, ISVZ, and
1292 OSVZ at P5.
1293

Figure.1. Cell types in developing ferret cerebral cortex.

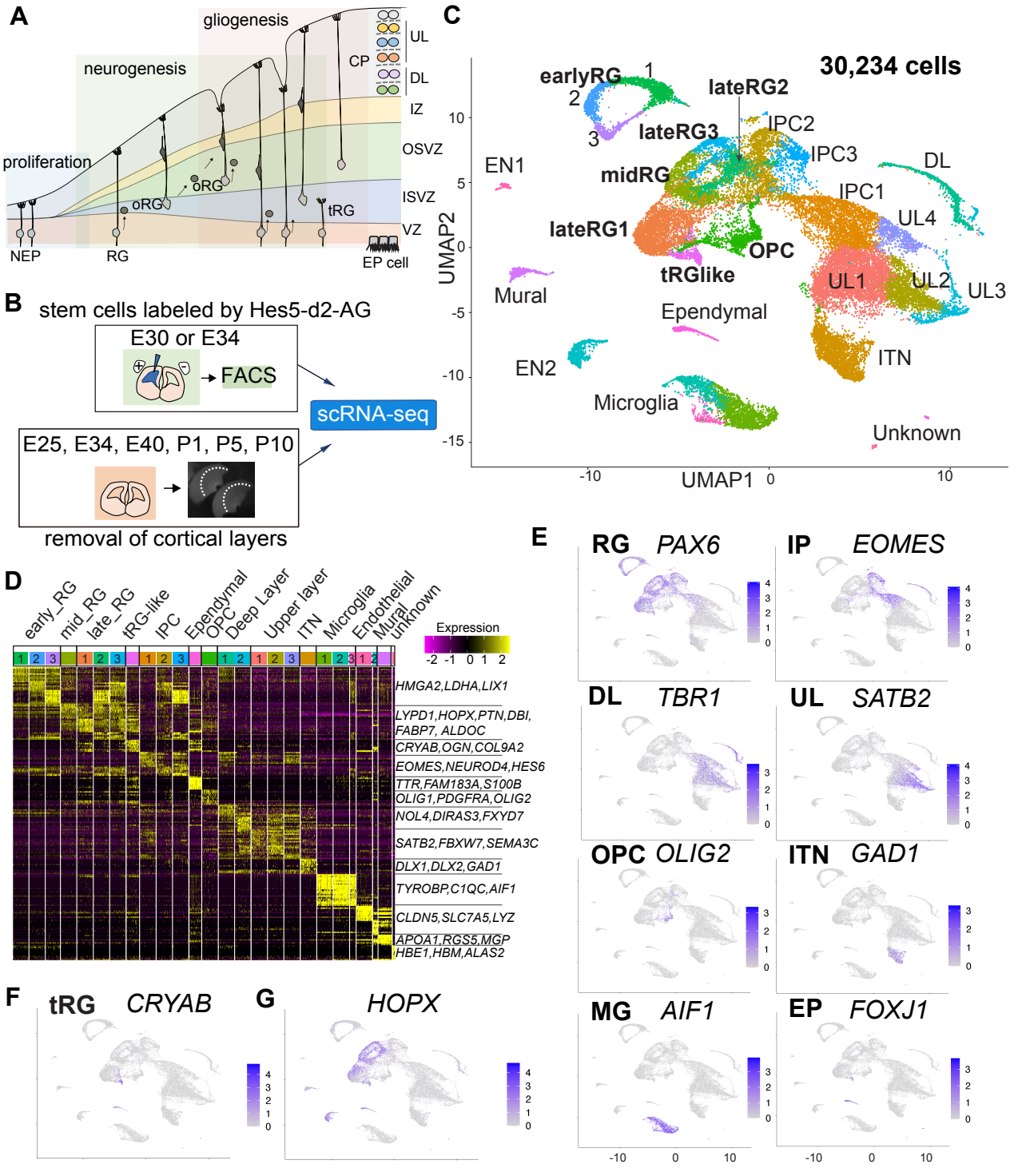

Figure 2. Emergence of ferret tRG during post-natal cortical development.

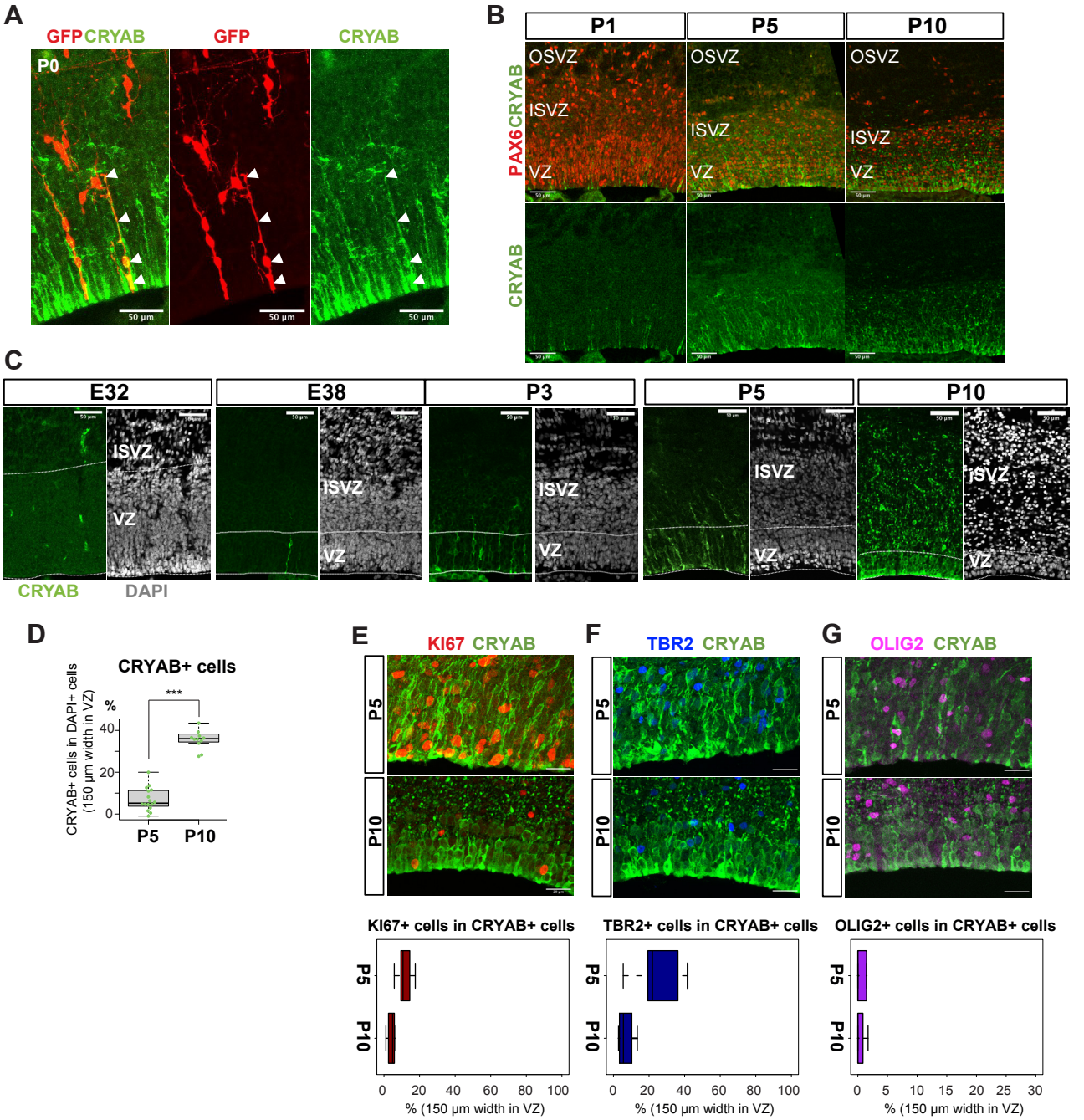

Figure 3. Emergence of ferret tRG during late embryonic cortical development.

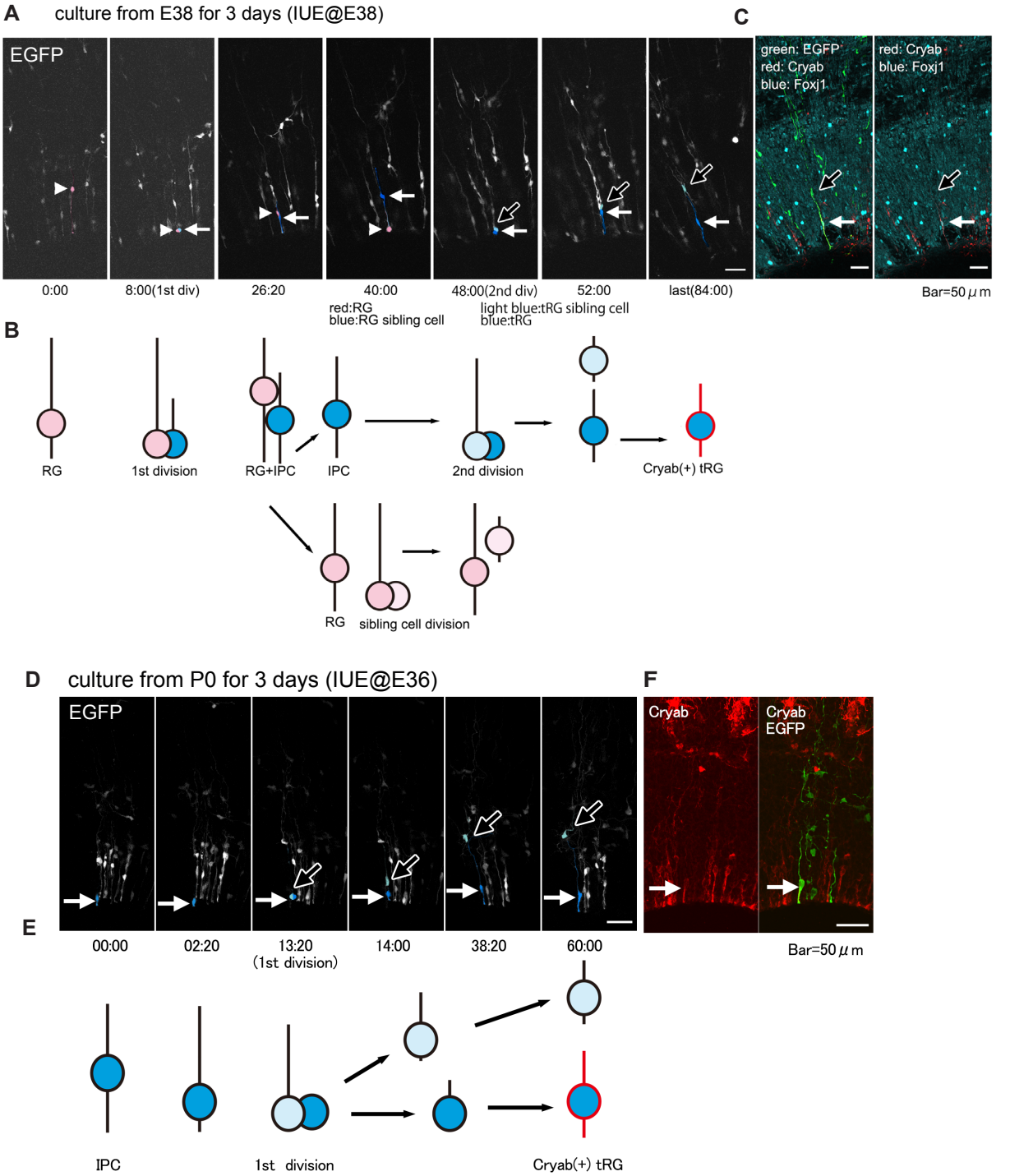

Figure 4. Temporal fates of RG cells predicted by pseudo-time trajectory analysis.

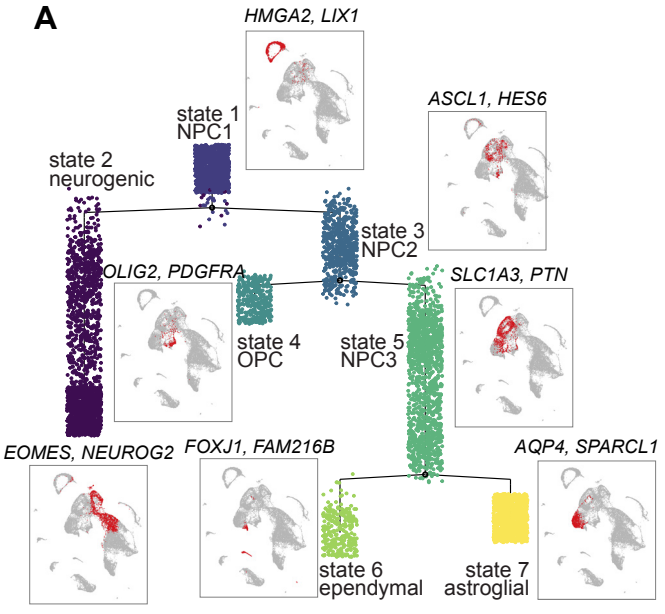

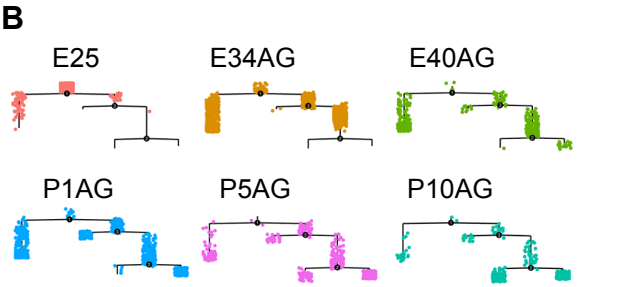

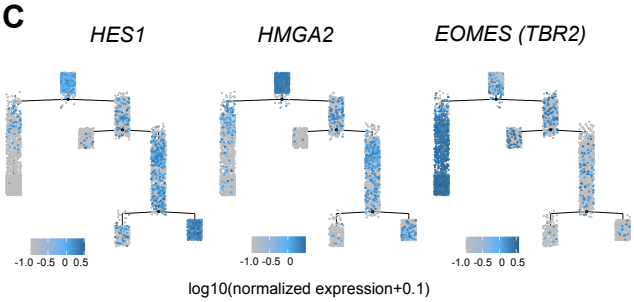

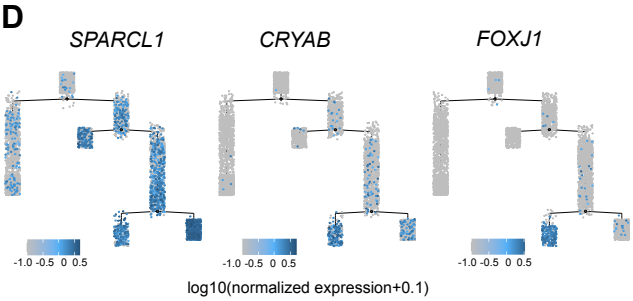

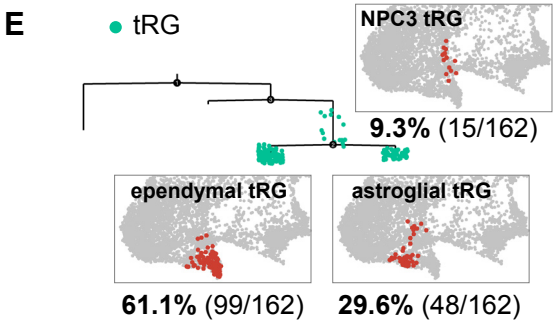

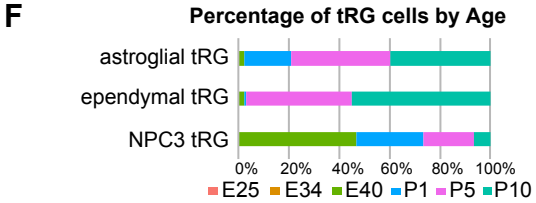

Figure 5. tRG adopt both ependymal and astrogenic fates in ferrets.

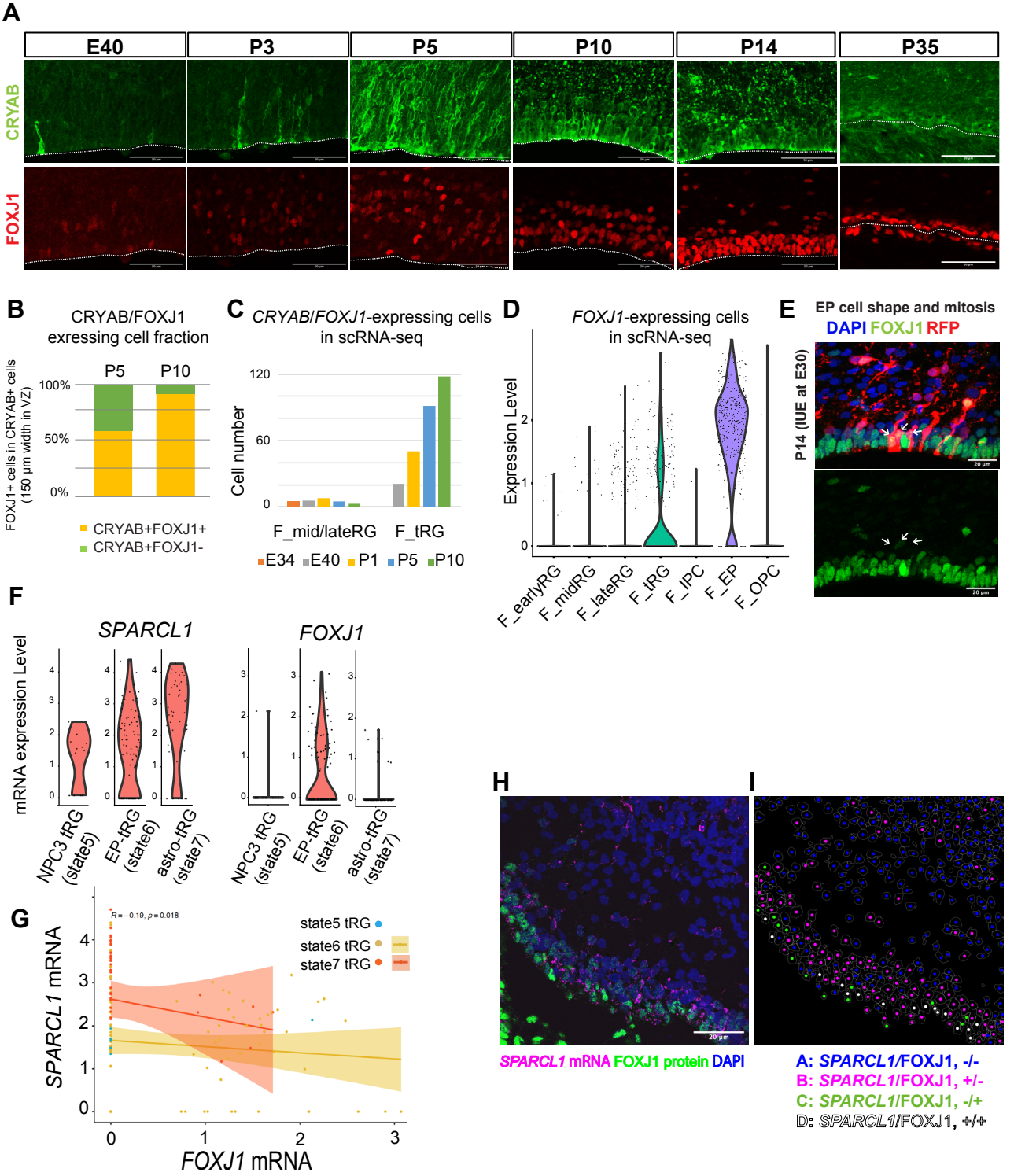

Figure 6. Comparison of molecular identity of RG subtypes between ferret and human.

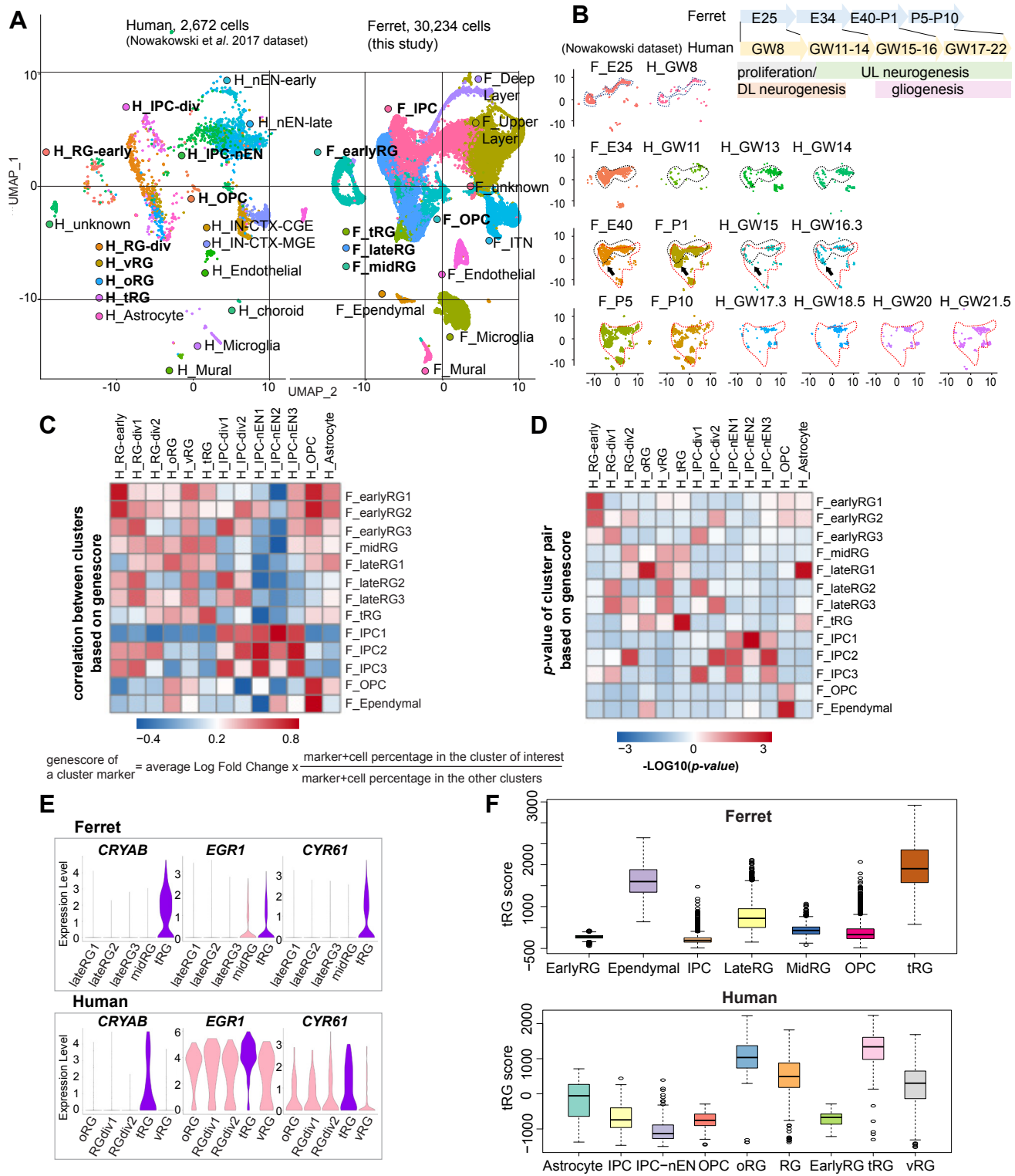

Figure 7. Comparison of the tRG and oRG subtypes between ferrets and humans.

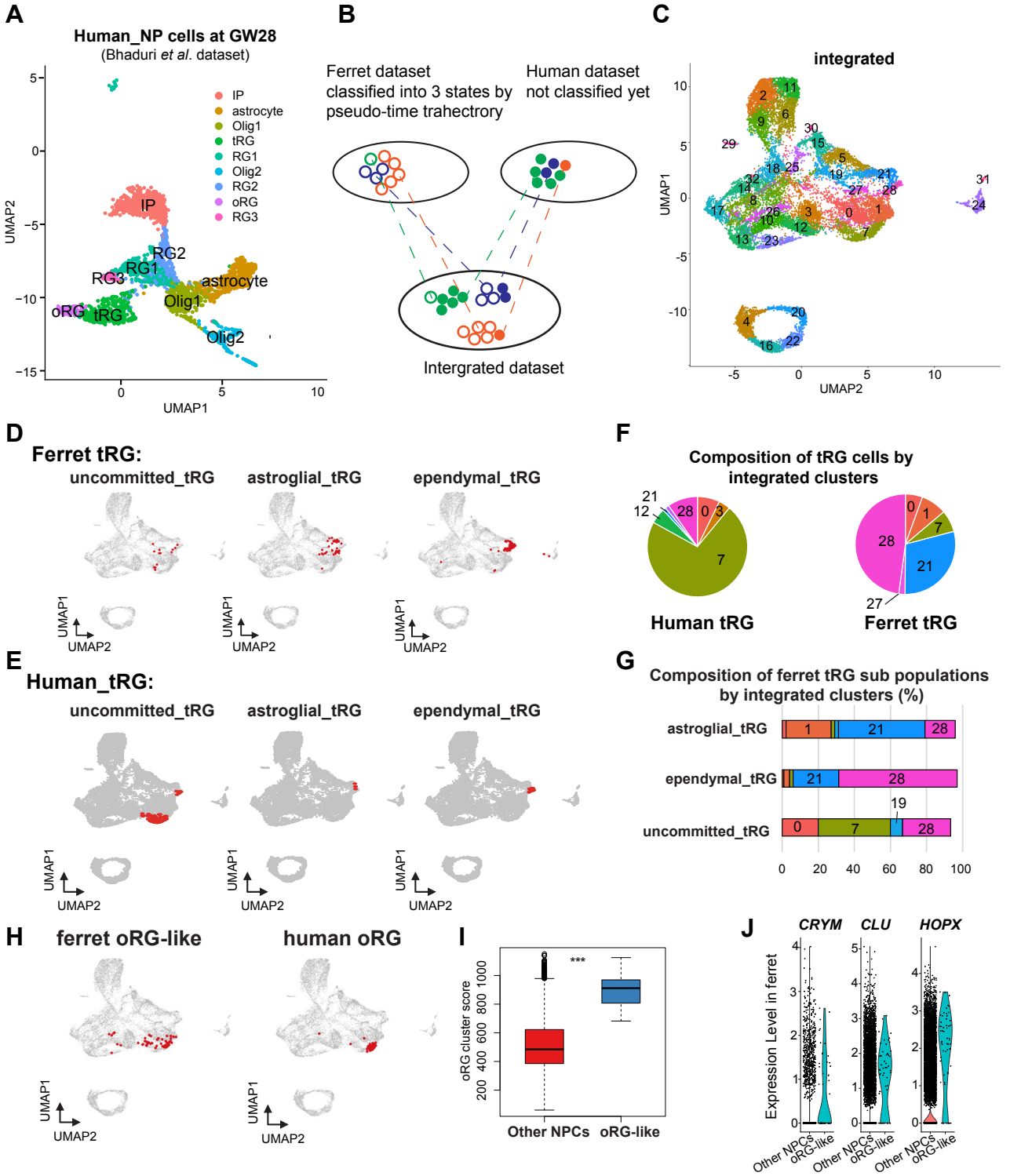

Figure S1. Development of the ferret cerebral cortex.

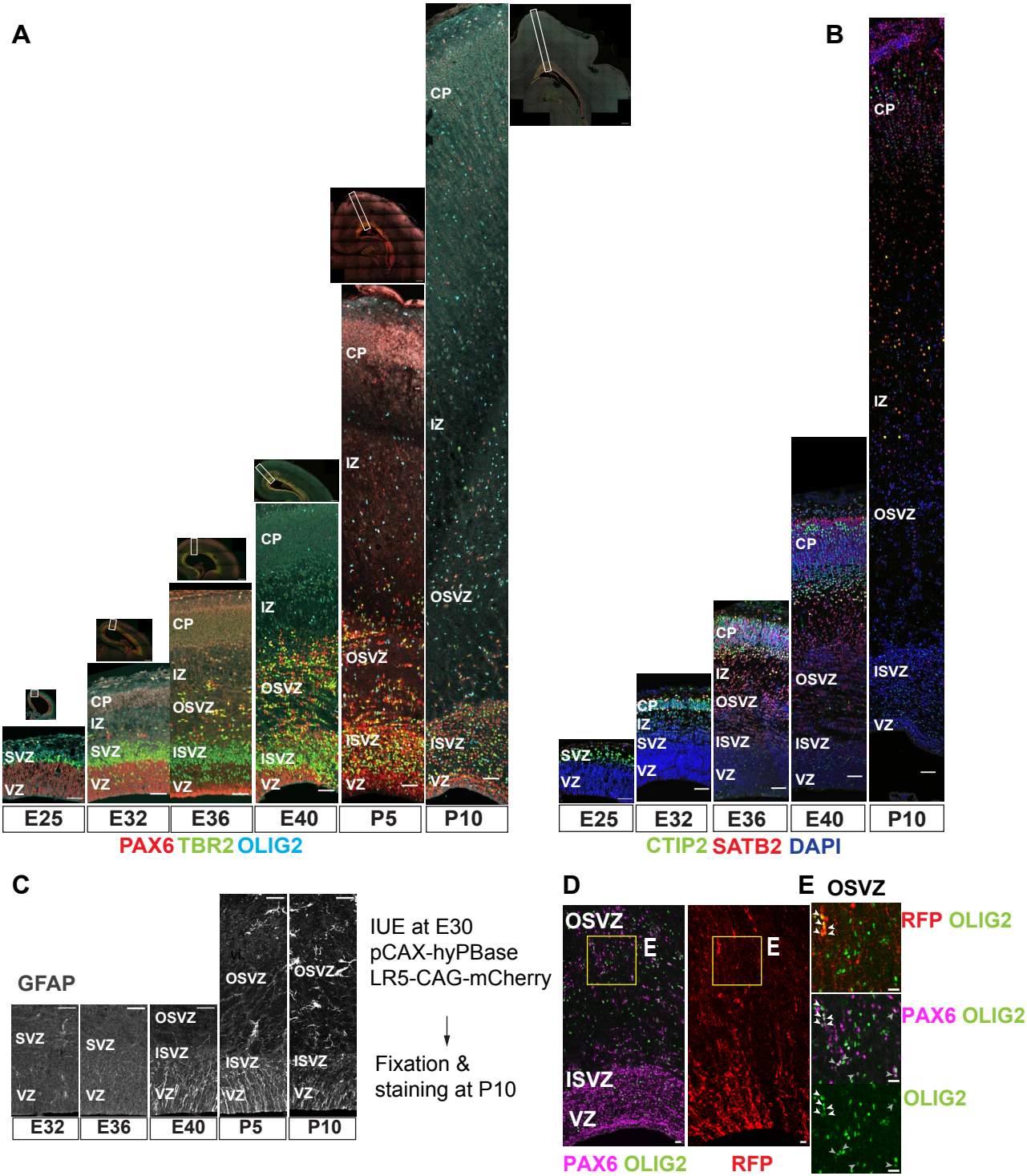

Figure S2. Cell types in developing ferret cerebral cortex.

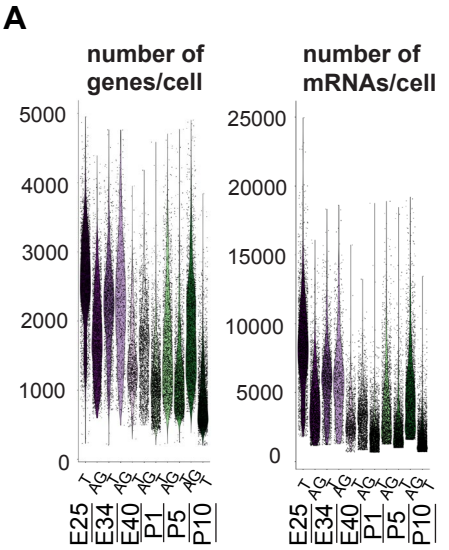

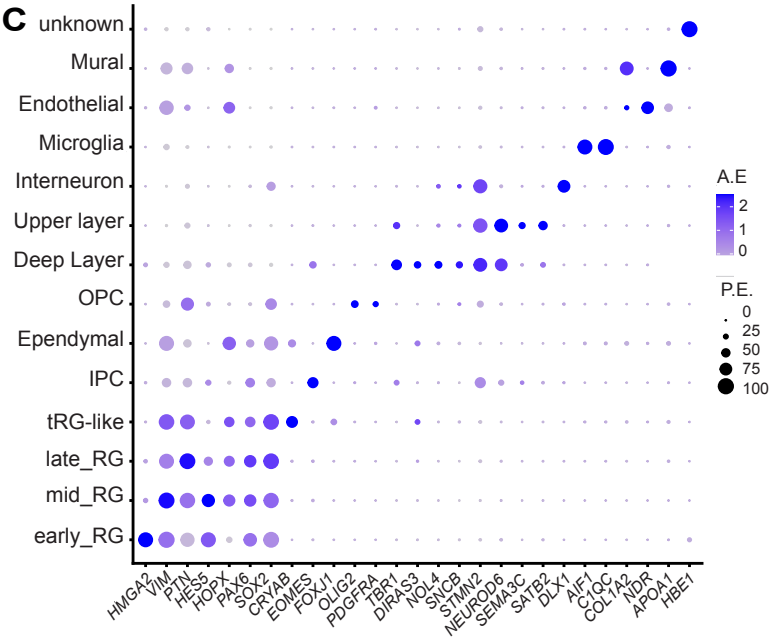

B

	Reference	Estimated Number of Cell	Median Genes per Cell	Number of Reads	Reads Mapped to Transcriptome	Total Genes Detected	Median UMI Counts
E34_AG	NCBI	3,226	953	137,673,935	30.70%	14,562	2,153
E34_AG	This study	3,223	1,763	137,673,935	58.20%	17,886	3,983
E34_T	NCBI	2,260	1,182	107,508,876	29.90%	14,445	3,096
E34_T	This study	2,265	2,195	107,508,876	56.40%	17,838	5,863

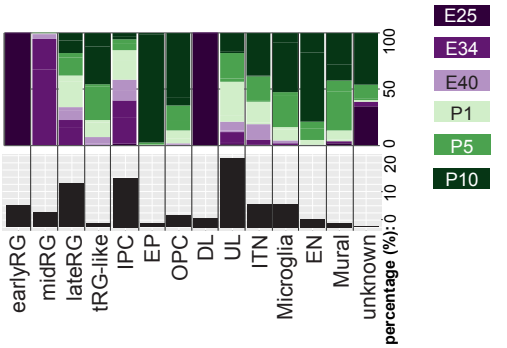

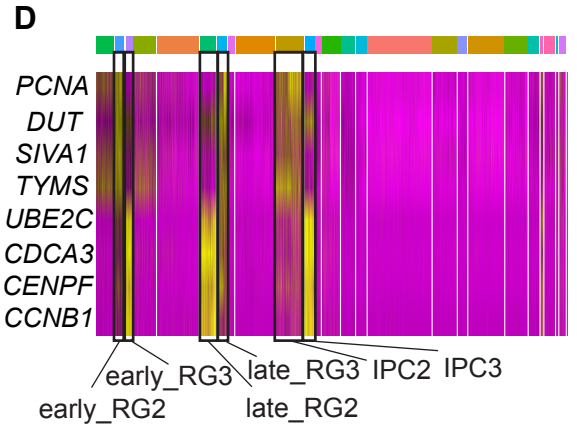

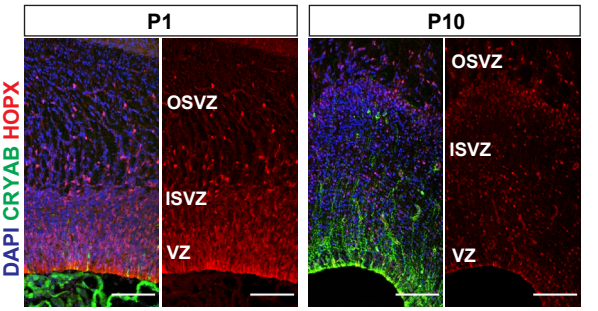

Figure S3. Development of ferret tRG during post-natal cortical development.

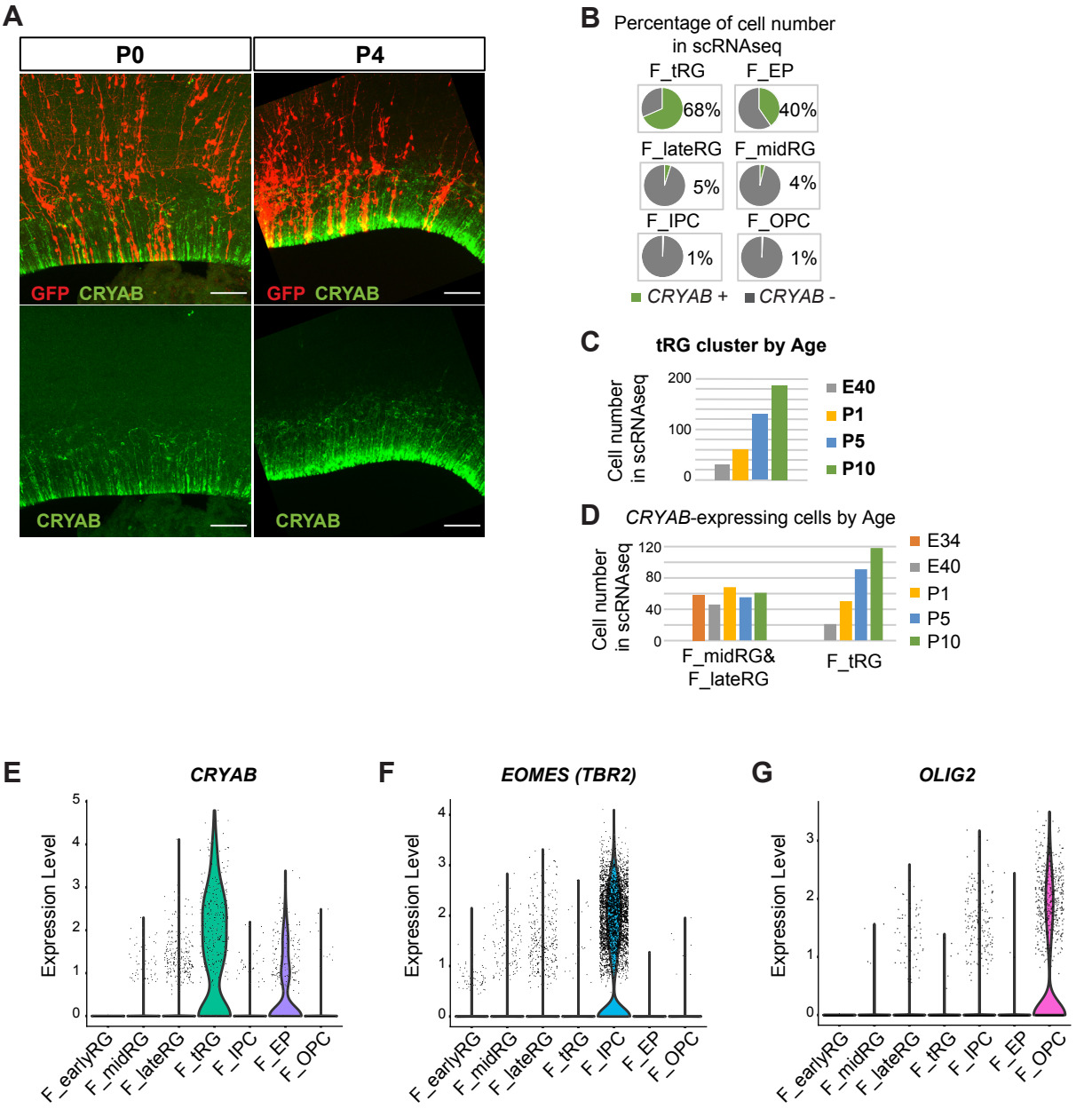

Figure S4. Temporal fates of RG cells predicted by pseudo-time trajectory analysis.

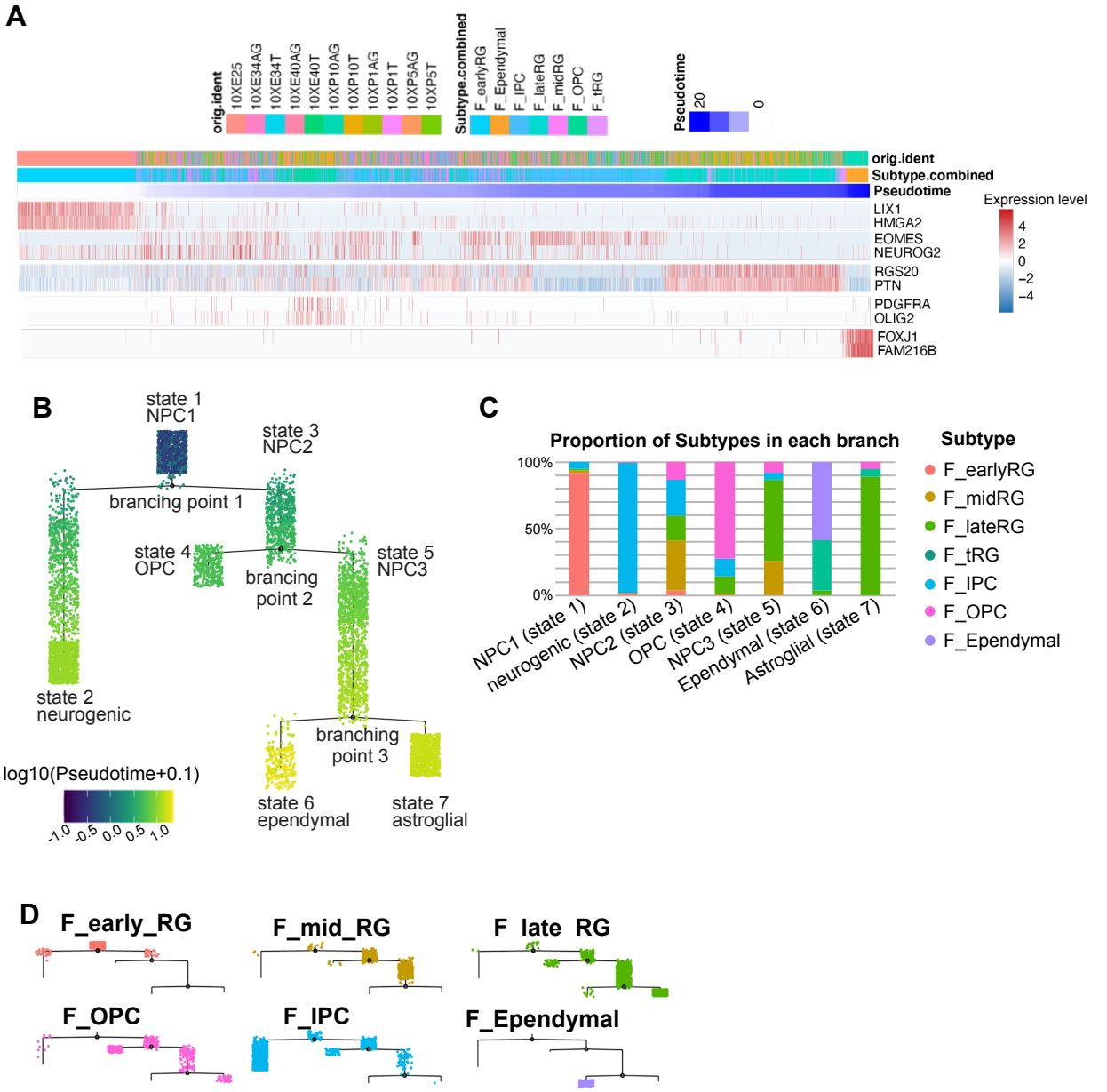

Figure S5. tRG adopt both ependymal and astrogenic fates in ferrets.

A

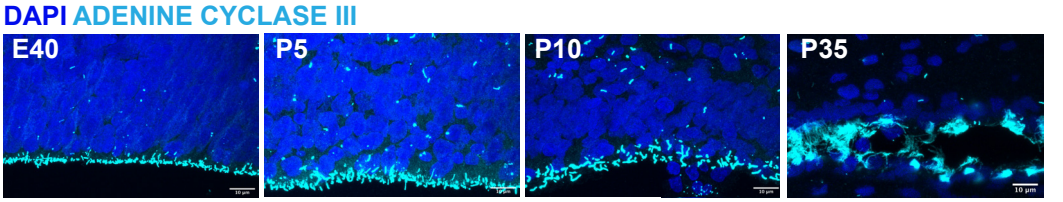

B

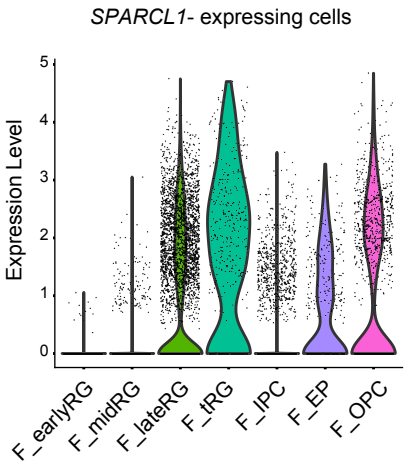

C

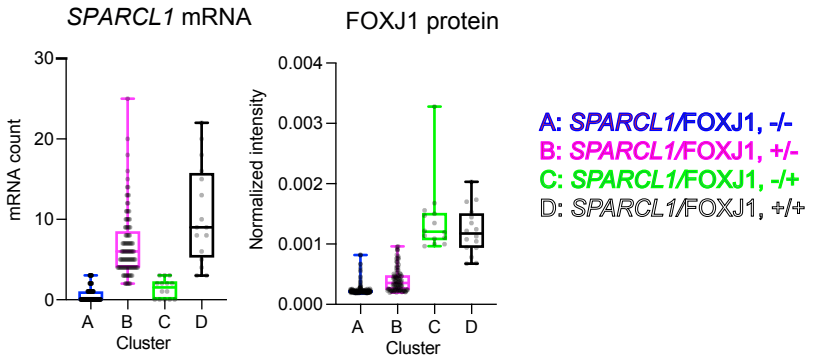

D

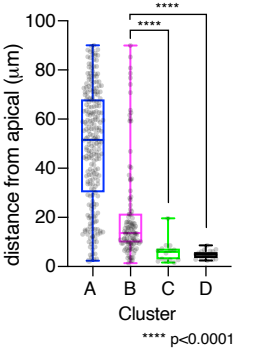

Figure S6. Comparison of molecular identity of RG subtypes between ferret and human.

A

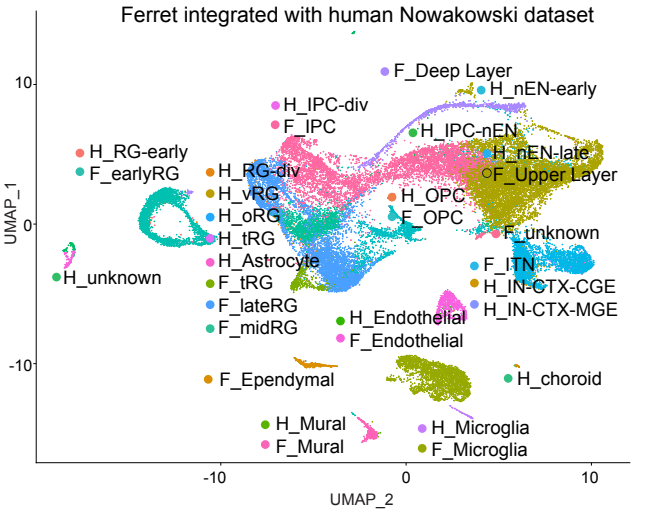

B

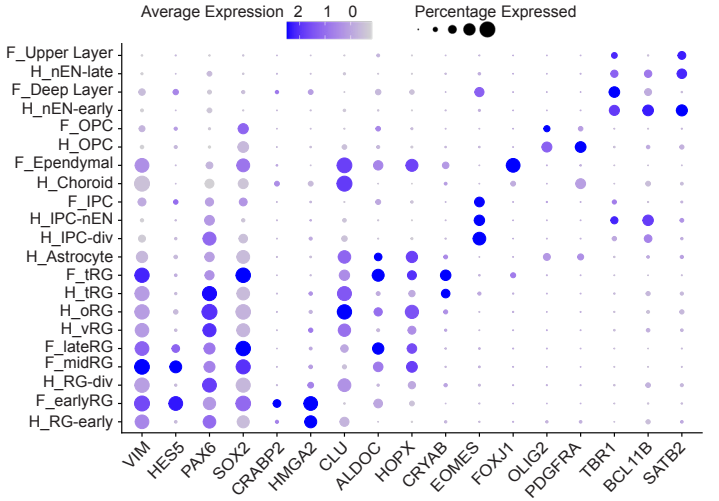
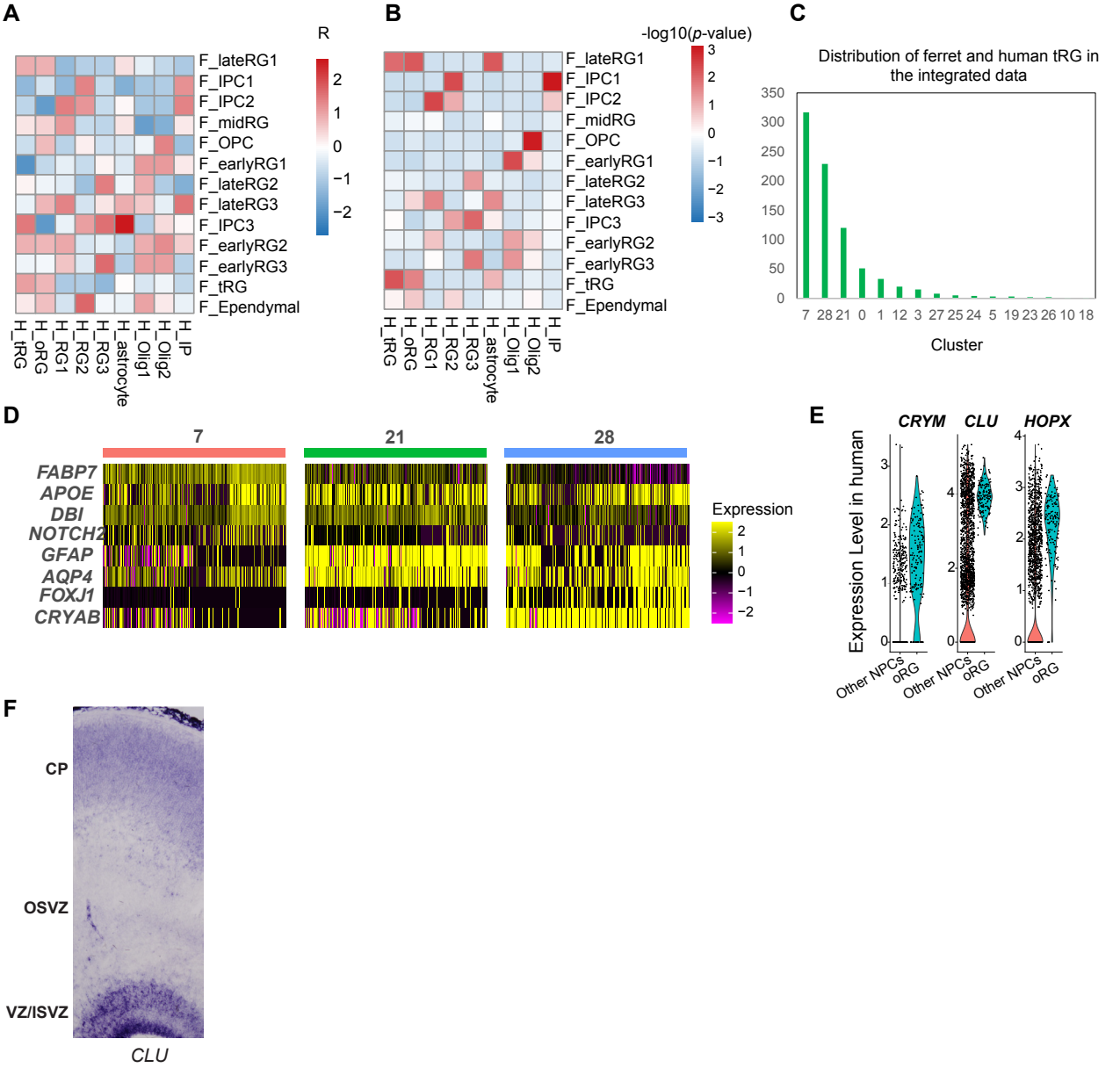
Figure S7. Comparison of the tRG and oRG subtypes between ferrets and humans.